OPTICALLY RELAYED PUSH-PULL VELOCITY INTERFEROMETRY
RESOLVED IN TIME AND POSITION

by

Dirk J. Robinson

A thesis submitted in partial fulfillment of

the requirements for the degree of

Master of Science in Physics

WASHINGTON STATE UNIVERSITY

Department of Physics

May 2005

To the Faculty of Washington State University:

The members of the Committee appointed to examine the thesis of DIRK J. ROBINSON find it satisfactory and recommend that it be accepted.

_____

Chair

_____

_____

ACKNOWLEDGMENTS

First, I would like to thank Dr. James Asay for his constant encouragement and support during the course of this work. He has regularly reserved time to discuss both the applications and techniques of line-VISAR, which kept my morale up and helped me not to narrow my focus too much. Dr. Asay has also shown a great commitment to helping me finish writing this thesis.

I thank Dr. Yogendra Gupta for taking the time with me to find a project that fit so neatly to my tastes and that has greatly expanded my problem-solving toolbox. Also, Dr. Gupta trusted me to bring an untested design to fruition. This project has made me appreciate the risk he took.

Kurt Zimmerman especially deserves recognition for the initial work on the line-VISAR. Several of the essential components were already on hand thanks to Kurt, including all of the long lead-time components. The motorized interferometer mirror was Kurt's idea, which has saved many hours. Another way Kurt was instrumental to the success of this work was that he took the time to understand the design workings and benefits at a time when few people could.

I would also like to thank my "laser gunner", Otto Berg. Otto helped develop the teflon-target for timing method. He also helped prepare and fire over 20 flyers on the laser-driven flyer apparatus, and he kept in good spirits despite initially discouraging results.

OPTICALLY RELAYED PUSH-PULL VELOCITY INTERFEROMETRY
RESOLVED IN TIME AND POSITION

Abstract

by Dirk J. Robinson, M.S.
Washington State University
May 2005

Chair: James R. Asay

A novel technique was developed to improve the spatial and velocity accuracy of line-VISAR. Specifically, a four-to-one optical relay was developed using open optics. Besides reducing the complexity, cost and alignment difficulty of true quadrature line-VISAR, the most precise type of line-VISAR, the relay technique provides unprecedented velocity and position resolution.

The VISAR equations which produce the velocity record from the interfered phase were re-derived around the concept of optical equivalence. This provides a more intuitive and general derivation, which allows for combinations of delay elements of different materials and accounts for individual path attenuations. A method for precisely obtaining optical equivalence by using white-light interference was also developed.

A new analysis program was written to complement quadrature push-pull line-VISAR instruments. This software makes use of multi-variable, nonlinear optimization to align the four quadrature images in time and position, under guidance from the user. An important element of the analysis software is a modified two-dimensional phase unwrapping technique. This modification automatically identifies a curve along which a fringe may need to be added. These automations greatly reduce the user effort and improve the accuracy of the analysis.

James R. Asay

TABLE OF CONTENTS

Appendix

LIST OF TABLES

LIST OF FIGURES

Appendix
Figure

NOMENCLATURE

beam dump A beam dump is a cavity designed to absorb as much incident light as possible. The beam dump used in this work had a reflective factor of under 10^{-4}.

GUI A Graphical User Interface, or GUI, is a part of a software program that allows a user to interact with the software in a graphical, event-driven manner.

optical equivalence Two systems are said to be optically equivalent if their mapping of position and angle with respect to the optical axis is identical. In particular, a glass element with parallel sides is optically equivalent to a shorter length of air.

path responsivity The combined gain of an optical path, representing all optical attenuations and the detector/camera response.

polarizing beamsplitter cube (PBC) An optical element which separates light into its polarization components. The horizontal component passes through the PBC without deflection, while the vertical component is reflected, typically at a right angle.

position lineout A curve obtained for a specific position on a data set surface, analogous to a time lineout

resolution Throughout this thesis, the term resolution is reserved for the number of distinct line-pairs that a system can resolve, either in position or time. For example, most digitizing oscilloscopes have better time resolution than streak cameras because of the number of data points available.

telecentric An optical system is said to telecentric if the cone of light it collects from an object has an axis of symmetry which is parallel to the optical axis. Telecentric systems are free from transverse distortions as the object plane moves.

temporal equivalence Two systems are said to be temporally equivalent with respect to a specific ray of light if the time the light takes to traverse the systems is equal. In particular, a glass element with parallel sides is temporally equivalent to a longer length of air, for a particular angle of incidence.

time lineout In a three-dimensional data set surface with the independent parameters of time and position, a time lineout is the curve along the surface for a specific time instant.

vignetting The attenuation of light caused by the light passing outside of lenses and other optical elements.

Chapter 1

Introduction

Light reflecting from a moving surface experiences a change in wavelength given by the Doppler effect[1]. When the angles of incidence and reflection of the light are close to the direction of motion, the wavelength is modified according to

$$\lambda(t) = \lambda_0 \left(1 - \frac{2v(t)}{c} \right),$$

(1.1)

where $\lambda(t), \lambda_0, v(t)$ and c denote the shifted wavelength, unshifted wavelength, velocity and the speed of light, respectively.

Typical shock experiments produce a relative change in wavelength of only about one part per million. Nevertheless, the wavelength shift may be accurately measured by interfering the reflected light with a delayed version of itself[2]. Originally, this was accomplished using Michaelson interferometers, which simply had one leg longer than the other by several centimeters. Since the two legs of the interferometer were not optically equivalent, only targets that maintained a mirror polish throughout the experiment could be used.

In 1972, L. M. Barker introduced the wide-angle Michaelson interferometer for shock wave experiments[3]. This interferometer uses glass delay elements (etalons) in one of the interferometer legs. With proper mirror spacing, the two legs can be made optically equivalent while having a transit time difference. Thus, it was possible to record velocities for surfaces that did not have a mirror polish or did not maintain the mirror finish throughout the experiment. The instrument was called a Velocity Interferometer System for Any Reflector (VISAR).

In 1990, W. Hemsing added position resolution to a very similar VISAR design, using a streak camera for recording[4]. Earlier in 1983, Sheffield and Bloomquist invented a simplified

system that interprets velocity from the displacement of a static fringe "comb" pattern, which is a spatial carrier wave[5]. The system was originally developed to record a single velocity point, taking advantage of a streak camera to record events on a sub-nanosecond time scale. Later, the system was extended to provide position resolution[6]. Both this system and the Hemsing system measure the velocity across a line illuminated on a target, so they are called line-VISARs. However, the fringe-displacement design is sometimes referred to as line-ORVIS, for Optically Recording Velocity Interferometry System.

1.1   Motivation

Many shock wave experiments do not have one-dimensional symmetry, spurring an interest for resolving velocity histories in both time and position. An important example is the study of heterogeous materials, where shock-wave interaction with the material is expected to produce velocity records which vary with position[7, 8]. Line-VISARs provide information on velocity variation with position that is critical to developing simulation models for heterogeneous materials. Another application is the characterization of new shock-wave generators such as laser-driven flyers. In this case, a line-VISAR can provide information on the planarity of the shock-waves that are produced.

1.2   Objectives and Approach

The goal of this work was to develop a line-VISAR for use at the Institute for Shock Physics at WSU. Prior to this work, line-VISARs had been developed and used only at National Laboratory facilities. The design requirements were that the system could be movable, with several available line lengths at the target, and the setup time should be short. The fringe displacement line-VISAR[6] seemed to meet these requirements, but the spatial and velocity resolution were low in comparison to the Hemsing design[4]. However, the Hemsing design relied on a four-to-one relay of coherent fiber bundles to record with a single streak camera. The fiber bundles

created alignment difficulties, and Hemsing reports that broken and misaligned fibers were a persistent problem[9].

In consequence, a new line-VISAR design was developed, following the Hemsing design. However, the four-to-one relay is implemented with a novel open-air optical relay. The work performed for this thesis includes the design, construction, and testing of this system, as well as the development of a highly automated software package for data analysis.

Chapter 2

Theoretical and Experimental Background

2.1   Velocity Interferometry

Velocity interferometers are based on the Michaelson interferometer design shown in Fig. 2.1. However, unlike a typical displacement sensing Michaelson interferometer, the interferometer mirror positions are fixed during the experiment. The two interferometer legs are set to have a difference in light transit time, making the interferometer sensitive to wavelength changes of the incident light.
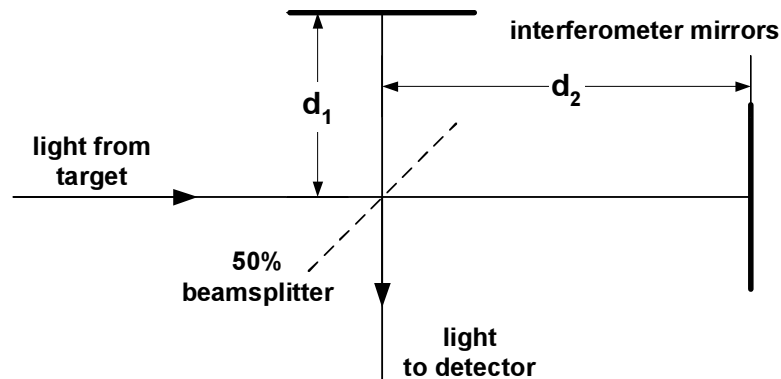
Figure 2.1 Simplified velocity interferometer

If narrow-band laser light is reflected from a moving target, the reflected light will be shifted in wavelength by the Doppler effect[1]. To find the magnitude of wavelength change, consider two consecutive crests of an incoming light wave and the instants at which these wave crests reflect from a target, as illustrated in Fig. 2.2. The target velocity, $u(t)$, is assumed to be constant over this time interval. Since both wave crests traverse a distance of $\lambda_0 - u(t)\Delta t$ during the interval Δt, the reflected wavelength is given by $\lambda(t) = \lambda_0 - 2u(t)\Delta t$. In typical

shock-wave experiments, $\left|\frac{u}{c}\right| < 10^{-5}$, so we can use the approximation $\Delta t = \frac{\lambda_0}{c}$. Using this approximation we obtain the Doppler wavelength shift:

$$-\frac{\Delta\lambda(t)}{\lambda_0} = \frac{2u(t)}{c} \tag{2.1}$$
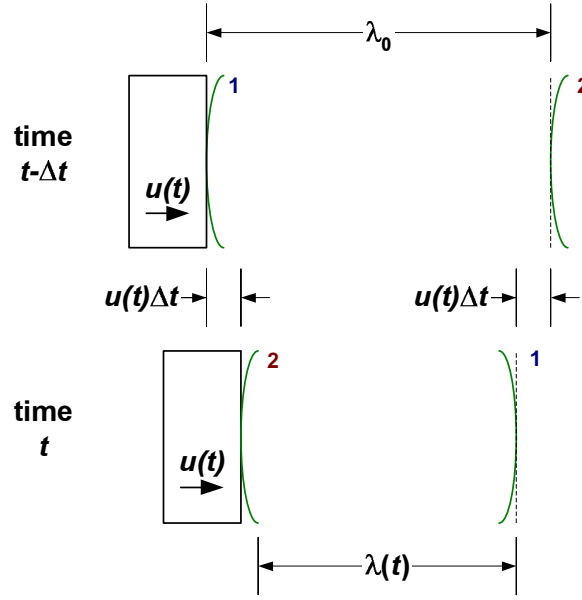
Figure 2.2 Doppler shift by considering light wave crests

A very simple velocity interferometer is shown in Fig. 2.1. Incoming light is split into two components, which then traverse the non-equal distances d_1 and d_2. Then, the components recombine and are sent to an intensity detector. The intensity at the detector follows the Michaelson interferometer equation[10]:

$$I(t) = \frac{I_0}{4}\left(1 + \cos\left(4\pi\frac{d_2 - d_1}{\lambda(t)}\right)\right) \tag{2.2}$$

The interfered phase, $4\pi\frac{d_2-d_1}{\lambda(t)}$, is sensitive to wavelength shift. From the wavelength shift, the target velocity can be recovered[2].

This analysis assumes that the target velocity remains constant over the time $2\frac{d_2-d_1}{c} \approx$ 1ns. W. F. Hemsing has shown that the actual phase response is reduced in bandwidth by a continuous average filter from the ideal response[11]. The temporal width of the filter is

$2\frac{d_2 - d_1}{c}$. Hemsing also showed that an inverse filter can be applied to remove this bandwidth limitation, but the technique dramatically reduces signal-to-noise ratio.

The type of velocity interferometer shown in Fig. 2.1 does not have optically equivalent legs, so it cannot be used in an imaging system. Without optical equivalence, the spatial coherence of the light must be very high. In consequence, this type of interferometer has the additional limitation that it can only be used with targets that have a mirror polish. In practice, this type of interferometer has been replaced VISARs, which use glass delay elements in one leg of the interferometer. The delay elements, or etalons, allow VISARs to simultaneously exhibit velocity sensitivity and optical equivalence.

2.2 Point-VISAR to Line-VISAR

Fig. 2.3 shows a simplified schematic for a quadrature push-pull point-VISAR. Quadrature VISARs employ a waveplate to create a phase delay of $90°$ between the horizontal and vertical polarizations. Usually, a $\lambda/8$ waveplate is used which gives the required phase delay difference after two passes of the light.

Two beams emerge from the main beamsplitter, which are separate in phase by exactly $180°$. Push-pull VISARs record both of these outputs, giving them near optimal light efficiency and high dynamic range. Quadrature VISAR systems rely on a waveplate to provide an additional phase delay of approximately $90°$ between the horizontal and vertical components of the output beams. The two effects combine to produce four output signals in quadrature. The quadrature signals have relative phase delays of $0°, 90°, 180°$ and $270°$, as shown in Fig. 2.3. Polarizing beamplitters are used at the output to separate pairs of polarization-encoded signals.

In the ideal situation, the phase can be extracted from the quadrature signals using an arctangent as shown in Fig. 2.3. The velocity is related to the phase by the velocity per fringe constant (*vpf*). Practical complications will be explored later in the chapter.
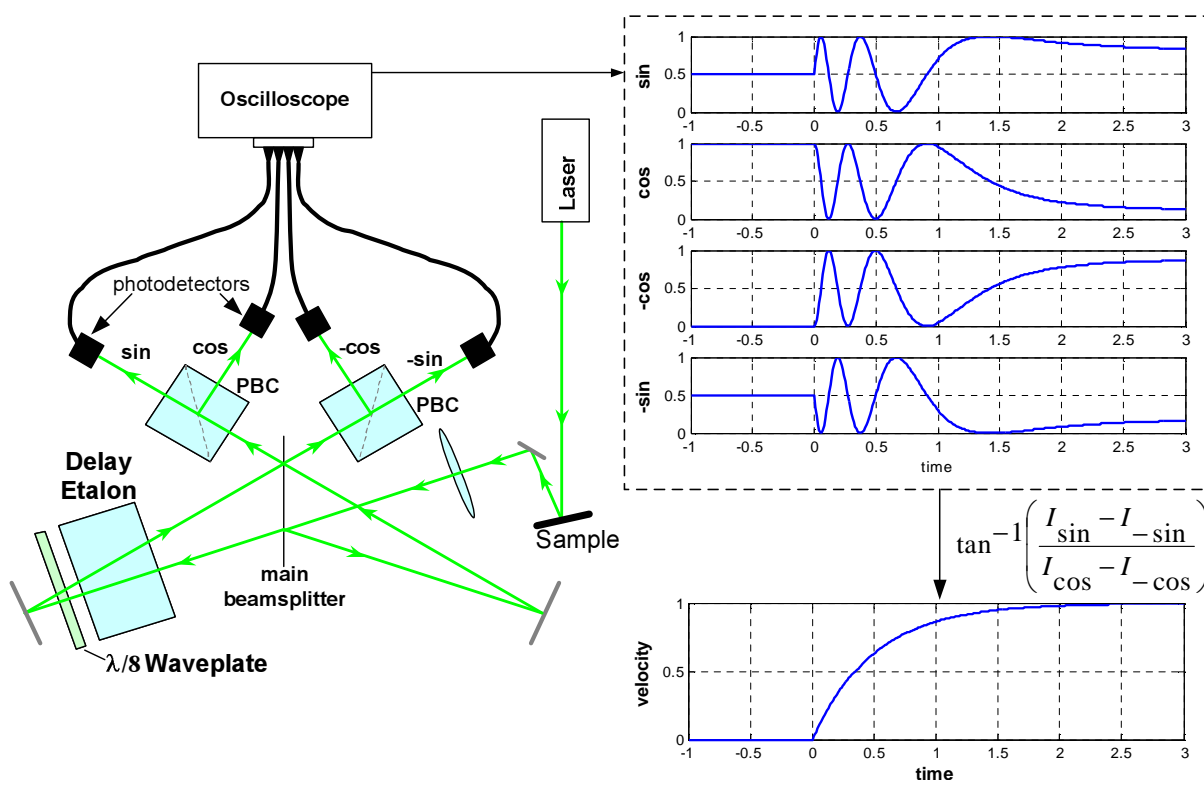
Figure 2.3 Quadrature Push-Pull Point-VISAR

2.2.1   Fringe-Displacement Line-VISAR

A fringe-displacement line-VISAR uses only one interfered image. This technique makes use of a spatial carrier frequency, or set of equally spaced interference fringes. This is referred to as a fringe comb. As the velocity changes, the interference fringes shift in position by a proportional amount, producing very intuitive image data records. This type of line-VISAR offers the easiest and most economical implementation.

To produce the spatial carrier, one of the mirrors in the interferometer is intentionally slightly misaligned by an angle α. Fig. 2.4 contains a schematic showing how the misaligned beams re-combine to produce the spatial carrier (left) and a typical recorded image from an experiment (right).
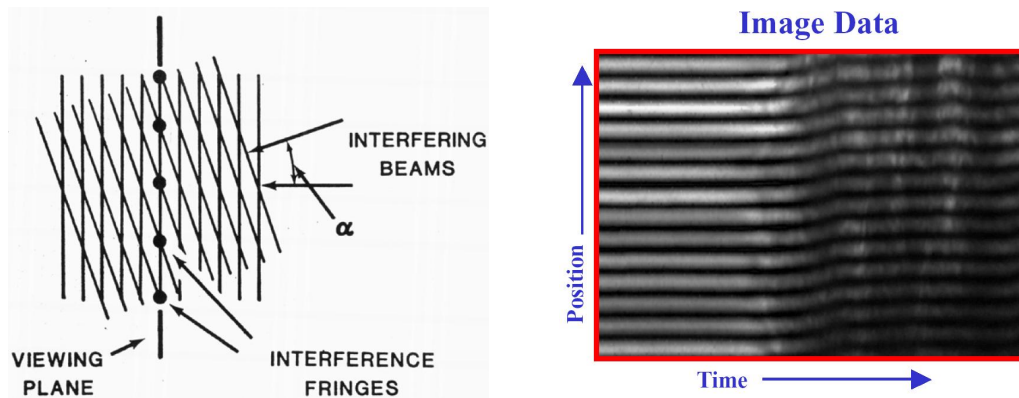
Figure 2.4 Fringe Displacement Line-VISAR [9]

The analysis of data taken from fringe-displacement VISAR designs usually involves taking time-lineouts separated in position with a spacing equal to $\frac{1}{4}$ of the spatial carrier wavelength[6]. Consecutive groups of four lineouts are then analyzed in a "pseudo-push-pull" method. This involves using the four lineouts as quadrature data channels in a single point analysis routine. An analysis technique using windowed Fourier transforms is also being investigated[9]. This method directly measures the displacement of the spatial carrier fringes, providing improved velocity accuracy.

The carrier wave used in the fringe-displacement technique imposes a trade-off between spatial resolution and velocity accuracy. A spatial carrier with a long wavelength results in a velocity accuracy similar to a quadrature push-pull system, but the spatial resolution is limited to approximately the carrier wavelength. Conversely, the technique approaches the spatial resolution of a quadrature push-pull system when a short carrier wavelength is used, but the velocity accuracy is greatly reduced.

2.2.2 Fiber-Relayed Push-Pull Line-VISAR

The fiber-relayed line-VISAR system was developed by W. F. Hemsing[4]. As shown in Fig. 2.5, the design is almost identical to single-point-VISAR designs, except that coherent fiber bundles are used to route the four quadrature images to a single streak camera.
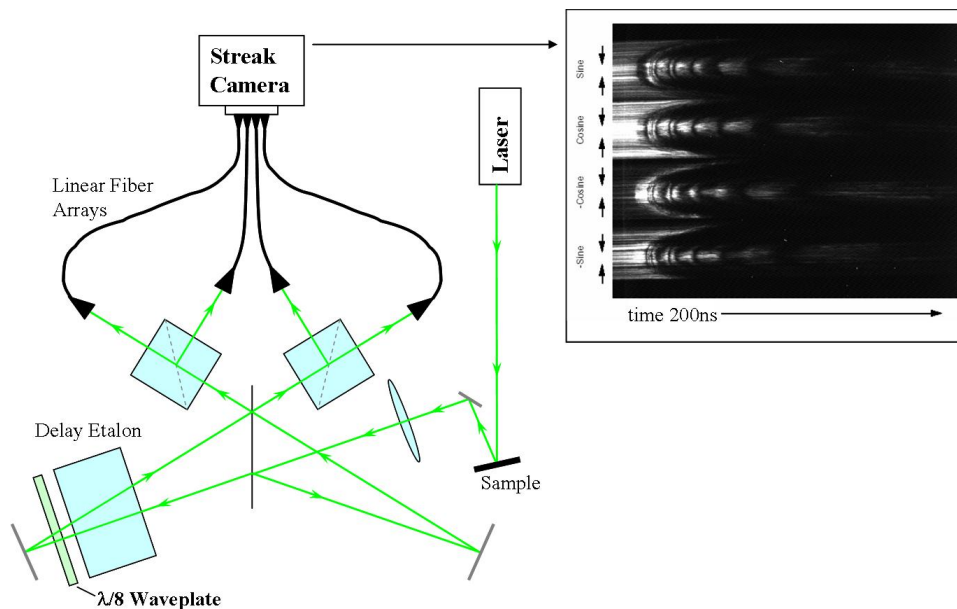
Figure 2.5 Fiber-Relayed Push-Pull Line-VISAR

This type of line-VISAR virtually eliminates sensitivity to laser speckle and other variations in the image intensity. Additionally, push-pull subtraction of the images effectively doubles the signal-to-noise ratio and eliminates the second-order nonlinearity of the detector response. However, variations in the path attenuations and camera sensitivity for the four images lead to

systematic velocity errors. The use of fiber bundles complicate these issues, as broken fibers create gaps in the images and produce a non-uniform warping of the images by different fiber bundles[9].

The Hemsing line-VISAR system should be capable of achieving velocity accuracies of 0.5-1.0% of the velocity-per-fringe constant, while simultaneously achieving near diffraction-limited resolution in position[9]. In comparison, the fringe-displacement technique has a velocity accuracy of 3-5% of the velocity-per-fringe[9]. However, fringe-displacement systems predominate in the field because of their ease of construction, alignment and analysis. To achieve high accuracy with a more user-friendly system, the Optically-Relayed Push-Pull line-VISAR was developed.

2.3   Optically-Relayed Push-Pull Line-VISAR

The Optically-Relayed Push-Pull line-VISAR uses a novel optical system to route the four interferometer outputs to the streak camera, as illustrated in Fig. 2.6. Similar to the Hemsing design, the light emerging from the interferometer must be separated into horizontal and vertical polarizations to recover the quadrature information. However, the new design uses only one beamsplitter to perform the separation by polarization of both interferometer outputs. In this manner, the collimated images overlap in pairs both before and after the beamsplitter. However, the pair partners are exchanged after the beamsplitter, so that each of the four turning mirrors reflects a unique pair of the quadrature images.

There remain too few degrees of freedom to place the images in any arbitrary arrangement. However, one possible arrangement is having the quadrature images in an equally spaced line, as shown in Fig. 2.6. This arrangement is well suited to line-VISAR.

2.4   VISAR Equations: Intensity to Velocity

This following derivation closely follows that of L. Barker and K. Schuler[12]. However, by centering the derivation on the concept of optical equivalence, the equations are generalized
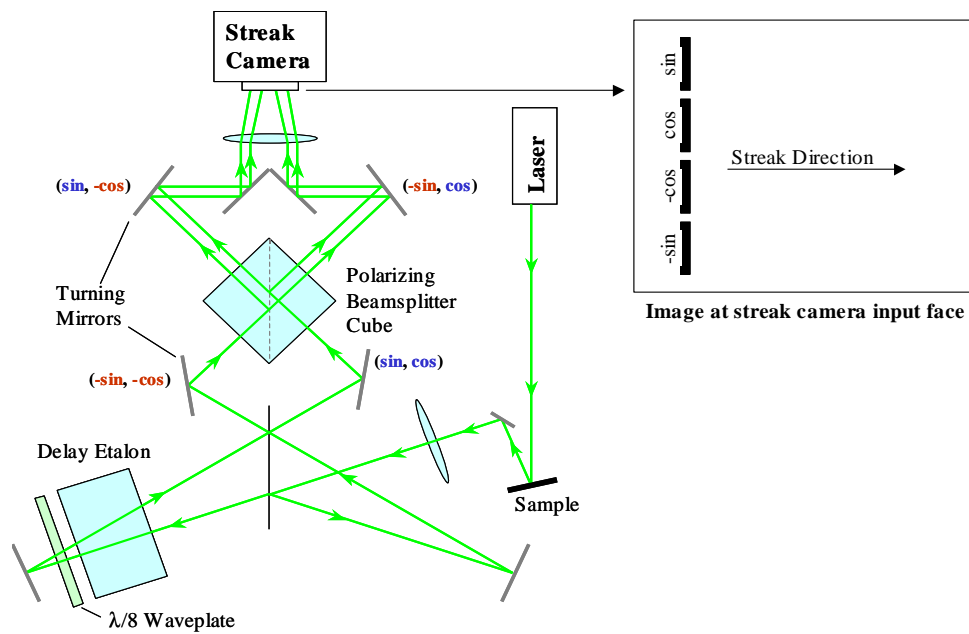
Figure 2.6 Optically-Relayed Push-Pull Line-VISAR

to allow different delay element materials to be used together. Also, the effect of angle of incidence is considered.

2.4.1 Time constant (τ)

The time constant, τ, is the difference in transit time between the two legs of the interferometer. A simple way to obtain τ is to consider the effect of inserting a single delay element. As shown in Fig. 2.7, the delay element of length L_i is optically equivalent to a space of air of length L_i/n_i, where n_i is the index of refraction of the delay element at the frequency of the probe laser. For a *single* pass of the beam, the transit time difference between the delay element and the equivalent air space is:

$$c\tau_i = n_i L_i \sec \theta_t - \frac{L_i}{n_i} \sec \theta_i \tag{2.3}$$
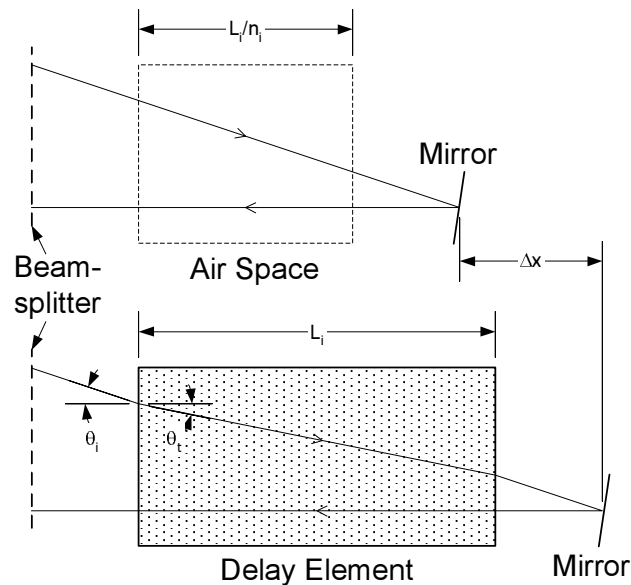
Figure 2.7 Delay element (bottom) and optically equivalent airspace (top)

One of the characteristics of optically equivalent systems is that focal planes are displaced only by the change in thickness of the two systems. In an interferometer system, maximum contrast is achieved when the two legs of the interferometer are optically equivalent. Thus, according to Fig. 2.7, in order to maintain maximum contrast after inserting a delay element

in one leg of the interferometer, the mirror on that leg must be moved by an amount $\Delta x = L_i \left(1 - \frac{1}{n_i} \right)$. Note that the direction of motion is normal to the surface of the delay element.

Now, consider a beam of light that makes N passes through delay elements, with indices n_i, and thicknesses L_i, where $i = 1, \cdots, N$. In a typical VISAR system, all of the delay elements are placed in one leg of the interferometer. The opposite leg has no delay elements, and its mirror position is set so that the two legs are optically equivalent. Thus the total transit time difference is the sum of the transit time difference for each pass through a delay element:

$$c\tau = c \sum_{i=1}^{N} \tau_i = \sum_{i=1}^{N} L_i \left(n_i \sec \theta_t - \frac{1}{n_i} \sec \theta_i \right) \tag{2.4}$$

The secant terms in Eq. 2.4 suggest a second-order dependence on angle, but in fact τ depends on the angle only to fourth-order in θ. Using the expansion $\sec \theta \approx 1 + \frac{\theta^2}{2} + \mathcal{O}(\theta^4)$ and Snell's law we have:

$$\left(n_i \sec \theta_t - \frac{1}{n_i} \sec \theta_i \right) \approx \left(n_i \left(1 + \frac{\theta_i^2}{2n_i^2} \right) - \frac{1}{n_i} \left(1 + \frac{\theta_i^2}{2} \right) \right) = \left(n_i - \frac{1}{n_i} \right) \tag{2.5}$$

Thus, the angular dependence of τ cancels to third-order. For the line-VISAR system discussed in this paper, when all the angles are taken into account, τ is increased by less than 0.01%. From this point forward, the angular dependence of the transit time will be dropped, reducing Eq. 2.3 to:

$$c\tau = c \sum_{i=1}^{N} \tau_i = \sum_{i=1}^{N} L_i \left(n_i - \frac{1}{n_i} \right) \tag{2.6}$$

2.4.2 Velocity per Fringe (*vpf*)

Now, we proceed to find the velocity per fringe constant (*vpf*). This is the change in velocity of the target which would result in exactly one fringe cycle at the camera/detector. The *vpf* calculation precedes the consideration of window materials in contact with the target[12].

To accurately determine the *vpf*, the dispersion of the delay elements, or dependence of the index of refraction on wavelength, must be considered[12]. Consequently, when the index of

refraction refers to a delay element, it is written as $n_i(\lambda(t))$. For convenience, the index of refraction at the laser wavelength, λ_0, will be simply written as n_i.

Let $N(t)$ denote the difference in the number of cycles of the recombining light beams at the interferometer output. $N(t)$ can be obtained from the transit time difference divided by the wavelength, $N(t) = c\tau(t)/\lambda(t)$. The target is assumed to be stationary at $t = 0$, and thus the "fringe count" is defined as $F(t) = N(t) - N(0)$. Using Eq. 2.6:

$$F(t) = \frac{1}{\lambda(t)} \sum_{i=1}^{N} \left[L_i n_i(\lambda(t)) - \frac{L_i}{n_i} \right] - \frac{1}{\lambda_0} \sum_{i=1}^{N} \left[L_i n_i - \frac{L_i}{n_i} \right] \tag{2.7}$$

Note that in the above expansion, only the first n_i is dependent on wavelength. The second n_i term represents an equivalent air space, while the third and fourth are associated with a stationary target. Taking in mind that ($\frac{\Delta\lambda(t)}{\lambda_0} \approx 10^{-6}$), we continue with a first-order Taylor expansion in wavelength:

$$F(t) = \frac{\lambda_0 - \lambda(t)}{\lambda^2} \sum_{i=1}^{N} \left[L_i n_i - \frac{L_i}{n_i} \right] + \frac{1}{\lambda_0} \sum_{i=1}^{N} \left[L_i \left. \frac{dn_i}{d\lambda} \right|_{\lambda_0} \Delta\lambda(t) \right] \tag{2.8}$$

Again using the expression for τ (Eq. 2.6), we obtain:

$$F(t) = -\frac{\Delta\lambda(t)}{\lambda^2} c\tau + \frac{\Delta\lambda(t)}{\lambda_0} \sum_{i=1}^{N} \left[L_i \left. \frac{dn_i}{d\lambda} \right|_{\lambda_0} \right] \tag{2.9}$$

Using Eq. 2.1, we can express $F(t)$ as a function of target velocity:

$$F(t) = \frac{2v(t)}{\lambda_0} \left[\tau - \frac{\lambda_0}{c} \sum_{i=1}^{N} \left. \frac{dn_i}{d\lambda} \right| - \lambda_0 \right] \tag{2.10}$$

The second term of Eq. 2.10 represents a correction for dispersion, which has a relative magnitude of 2-4%. By convention, this term is written in terms of the "dispersion index", $\delta = -\frac{n}{n^2-1} \lambda_0 \left. \frac{dn}{d\lambda} \right|_{\lambda_0}$. This results in:

$$F(t) = \frac{2v(t)}{\lambda_0} \left[\tau - \frac{1}{c} \sum_{i=1}^{N} L_i \left(n_i - \frac{1}{n_i} \right) \delta_i \right] \tag{2.11}$$

Finally, we have the velocity per fringe constant:

$$vpf = \frac{v(t)}{F(t)} = \frac{\lambda_0}{2}\left[\tau + \frac{1}{c}\sum_{i=1}^{N} L_i\frac{n_i^2 - 1}{n_i}\delta_i\right]^{-1} \tag{2.12}$$

In general, the waveplate, etalons and main beamsplitter all act as delaying elements in the same interferometer leg, and may be of different materials. In fact, the waveplate is usually a different material but is thin enough to neglect its dispersion contribution. Thus, if all etalons and the main beamsplitter are of the same material, then the approximation $\delta_i = \delta = $ constant may be used. This yields the historical expression:

$$vpf = \frac{\lambda_0}{2\tau(1 + \delta)} \tag{2.13}$$

2.4.3   Consideration of Path Attenuations

It was observed that the components of the recombined images varied in intensity. In response, the line-VISAR analysis expands on previous work to account for different path responsivities, which includes the optical path attenuations and camera sensitivity. Consider the interference equation for the second (cos) quadrature image[10]:

$$I_2(t,y) = I_{2R}(t,y) + I_{2L}(t,y) + 2\sqrt{I_{2R}(t,y)I_{2L}(t,y)}C(t,y)\cos(\theta(t,y)) \tag{2.14}$$

Here, $I_{2R}(t,y)$ refers to the image component that traveled through the right interferometer leg, and $I_{2L}(t,y)$ refers to the left interferometer leg. $C(t,y)$ denotes the fringe contrast, which is a number between 0 and 1. Finally, $\theta(t,y)$ denotes the phase difference between the recombined images. From this point forward, the parameters (t,y) will be dropped for convenience.

Table 2.1 gives the actual phase differences between the components of the quadrature images. The associated quadrature images are shown in the example data of Fig. 2.8. ϕ denotes an extra phase offset from the waveplate. This offset is usually tuned to near zero by rotating the waveplate.

The component intensities are related by introduction of individual path attenuations R_i, L_i, shown below in Eq. 2.15. The four attenuations R_i are found by blocking the left leg of the
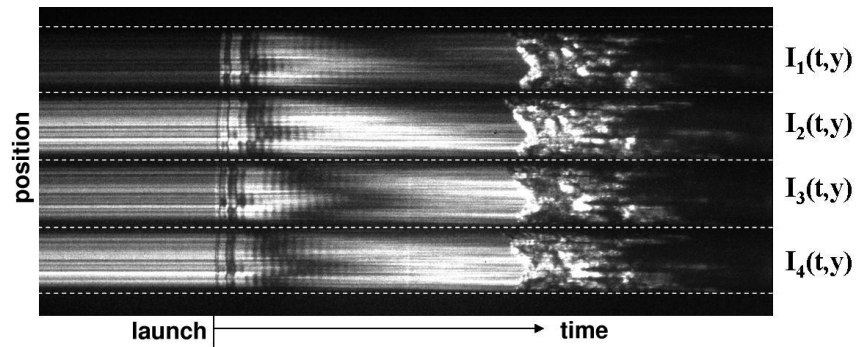
Figure 2.8 Quadrature streak images

Table 2.1 Phase offsets of quadrature images

Image	Phase Offset	Nominal
$I_1(t, y)$	$90° + \phi$	$\sin$
$I_2(t, y)$	$0°$	$\cos$
$I_3(t, y)$	$180°$	$-\cos$
$I_4(t, y)$	$270° + \phi$	$-\sin$

interferometer and recording the relative intensities of each of the four non-interfered images. Similarly L_i are found by blocking the right leg of the interferometer.

$$
\begin{aligned}
I_{1R} &= R_1 I_0 & I_{1L} &= L_1 I_0 \\
I_{2R} &= R_2 I_0 & I_{2L} &= L_2 I_0 \\
I_{3R} &= R_3 I_0 & I_{3L} &= L_3 I_0 \\
I_{4R} &= R_4 I_0 & I_{4L} &= L_4 I_0
\end{aligned}
\tag{2.15}
$$

Consideration of the individual path attenuations and the phase offsets from Table 2.1 leads to the following interfered intensities:

$$
I_1 = I_0 \left[R_1 + L_1 + 2\sqrt{R_1 L_1} C \sin(\theta + \phi) \right]
\tag{2.16}
$$

$$
I_2 = I_0 \left[R_2 + L_2 + 2\sqrt{R_2 L_2} C \cos(\theta) \right]
\tag{2.17}
$$

$$
I_3 = I_0 \left[R_3 + L_3 + 2\sqrt{R_3 L_3} C \left(-\cos(\theta) \right) \right]
\tag{2.18}
$$

$$
I_4 = I_0 \left[R_4 + L_4 + 2\sqrt{R_4 L_4} C \left(-\sin(\theta + \phi) \right) \right]
\tag{2.19}
$$

To recover the phase information, it is useful to define X and Y, the weighted cosine and sine differences:

$$
X = 2C I_0 \cos\theta = \frac{(R_3 + L_3)I_2 - (R_2 + L_2)I_3}{(R_3 + L_3)\sqrt{R_2 L_2} + (R_2 + L_2)\sqrt{R_3 L_3}}
\tag{2.20}
$$

$$
Y = 2C I_0 \sin(\theta + \phi) = \frac{(R_4 + L_4)I_1 - (R_1 + L_1)I_4}{(R_4 + L_4)\sqrt{R_1 L_1} + (R_1 + L_1)\sqrt{R_4 L_4}}
\tag{2.21}
$$

Additionally, define $I_{0_{\cos}}$ and $I_{0_{\sin}}$, the weighted cosine and sine sums. The image intensity, I_0, is defined as the average of these two quantities.

$$
I_{0_{\cos}} = \frac{\sqrt{R_3 L_3} I_2 + \sqrt{R_2 L_2} I_3}{\sqrt{R_3 L_3}(R_2 + L_2) + \sqrt{R_2 L_2}(R_3 + L_3)}
\tag{2.22}
$$

$$
I_{0_{\sin}} = \frac{\sqrt{R_4 L_4} I_1 + \sqrt{R_1 L_1} I_4}{\sqrt{R_4 L_4}(R_1 + L_1) + \sqrt{R_1 L_1}(R_4 + L_4)}
\tag{2.23}
$$

$$
I_0 = \frac{I_{0_{\cos}} + I_{0_{\sin}}}{2}
\tag{2.24}
$$

Using Eq. 2.24, we can extract the phase and fringe contrast from Eqs. 2.20 and 2.21, resulting in:

$$\theta = \tan^{-1}\left(\frac{Y - X\sin\phi}{X\cos\phi}\right) \tag{2.25}$$

$$C = \frac{\sec\phi}{2I_0}\sqrt{X^2 + Y^2 - 2XY\sin\phi} \tag{2.26}$$

The velocity is proportional to the phase by the velocity-per-fringe constant.The fringe contrast is also useful because it provides a measure of velocity variation at a finer scale than the position resolution. However, the apparent contrast also varies because of the time response of the recording device.

Chapter 3

Experimental Technique

3.1 Design

A scale drawing of the WSU line-VISAR is shown in Fig. 3.1. The design uses a smaller optical breadboard as a top level, which makes the design compact and easily movable. The following list details the components in Fig. 3.1 which are marked by diamond-surrounded letters, following the path of the laser light.

A. **Verdi Laser.** The source laser for the line-VISAR is a *Verdi* model manufactured by Coherent Inc. The output wavelength is 533 nm with a continuous output at an adjustable power level of 10 mW to 10 W. The output light is predominantly vertically polarized. The beam waist was measured to be approximately 2.3 mm.

B. **Acousto-optic modulator (AOM).** This device uses an acoustically generated diffraction grating to slightly deflect the beam. When aligned properly, almost all light intensity is diffracted to the first-order mode when the AOM is on.

C. **Iris.** An iris allows only the first-order mode from the AOM. A section of black plastic pipe was placed around the entrance of the iris to absorb scattered light form the zero-order mode. The zero-order mode corresponds with the off-state of the AOM.

D. **λ/2 waveplate.** This waveplate is used to convert the light polarization from vertical to horizontal.

Top Level

Setup Camera

Streak Camera

CCD

300 mm fl lens and flipping-mirror

Bottom Level

60"

30"

λ/2 Waveplate — D

Iris — C

Support Pillar (4)

λ/4 Waveplate

P.B.S.

Line-Forming Cylindrical Lenses — F

Aperture Stop

λ/2 Waveplate

Image Aperture

Acousto-optic Modulator — B

Verdi Laser

Beam Expansion — E

Periscope Beam Rotation and final lens — N

Right-Angle Reflector — M

Polarizing Beam Splitter — L

300mm fl lens

10°

alternate lens, 600mm — H

A

Potential Secondary Input (fiducial)

45.0°

15.0°

λ/8 Waveplate

Etalons

Main Beam Splitter — I

Motorized Interferometer Mirror — J

Stationary Interferometer Mirror — K

To Target

Figure 3.1 Schematic of WSU line-VISAR system

From Laser

Vertical Cyl. Lens 50mm fl

50mm

Virtual Image Aperture

Beam Dump

Kinematic Platform

From/To Target

λ/4 waveplate

Horizontal Cyl. Lens 100mm fl

100mm

Virtual Aperture Stop

λ/2 waveplate

1" Polarizing Beamsplitter Cube

Input Aperture Stop (Iris)

Image Aperture (Adjustable Slit)

To Interferometer Cavity
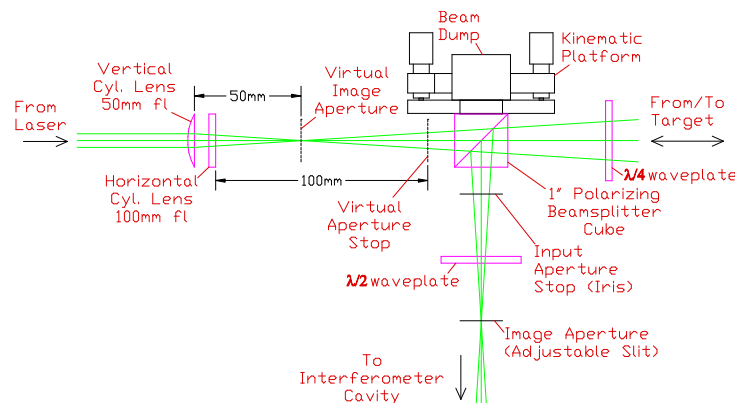
Figure 3.2 Input optics

E. **Beam expansion.** A pair of plano-convex lenses are used to expand the beam waist to approximately 4 mm. The spacing of this pair is used to adjust the length of the illuminated line.

F. **Input optics section.** This group of optics forms an image of the laser-illuminated line that will be relayed to the target. The input section also routes light to and from the target and routes the light to the interferometer section. It is discussed in more detail in the following section.

G. **Target-to-table relay.** A number of relays of different magnification are available, which serve to illuminate the target as well as collect light from it. They will be discussed in detail.

H. **Collimating lens.** A collimating optical system is one which maps points at the input image plane to parallel beams at a specific angle. A 300 mm achromatic lens is used to collimate the light before the interferometer. A 600 mm lens is also available, which reduces the magnification by 50%. However, the input section must be modified to support an intermediate image of the line that is double in length, as described later.

I. **Main beamsplitter.** This is a 50% beamsplitter, unlike the other two *polarizing* beamsplitters. The input beam is split into two parts. The left-going beam recombines with a delayed version of the right-going beam, which gives the interferometer sensitivity to Doppler frequency shifts.

J. **Right interferometer leg.** This leg contains a mirror that is tilted using piezo-electric motors. This is very useful when optimizing the interference pattern. Since it is operated by remote control, it is not necessary to touch the mirror mount itself, leading to a much more steady image. This mirror is also on a translation stage that adjusts for the number of etalons used. All elements which contribute a delay are placed on this side, including the substrate side of the main beamsplitter.

K. **Left interferometer leg.** This leg serves as a reference to the other. The mirror is moved only during re-alignment.

L. **Polarizing Beamsplitter Cube (PBC).** The use of a single output PBC with light incident on both faces is a novel feature of this design. This allows two pairs of beams to overlap spatially until they reach the final focusing lens.

M. **Right-angle Reflector.** A pair of mirrors were cut at a $45°$ angle and mounted as shown to create this reflector.

N. **Periscope.** The periscope consists of a mirror at the bottom, the final focusing lens aligned horizontally at the middle, and the flipping mirror at the top.

The top platform holds the setup camera and streak camera, with a flipping mirror to switch between them. The flipping mirror mount was custom made and holds a three-inch mirror. A spring is used to hold the mount against two locking set screws, routing the output to either the setup camera or the streak camera.

3.1.1 Input Optics

An image aperture and image cone aperture combination are central to the WSU line-VISAR design. The image aperture ensures good time resolution and prevents the quadrature images from overlapping at the camera image plane. Meanwhile, the input cone aperture limits the acceptance angle of the light into the interferometer to eliminate vignetting from mirror edges that may vary for the four images.

The input optics section (Fig. 3.2) takes advantage of the polarization of the laser light so that the same relay may be used to illuminate the sample and collect light from it. The polarization at an instant in time is graphically depicted in Fig. 3.3, which corresponds to the following detailed description:

1. The *Verdi* laser emits light which is mostly vertically polarized.

2. Light is converted to horizontal polarization using a $\frac{\lambda}{2}$ waveplate.
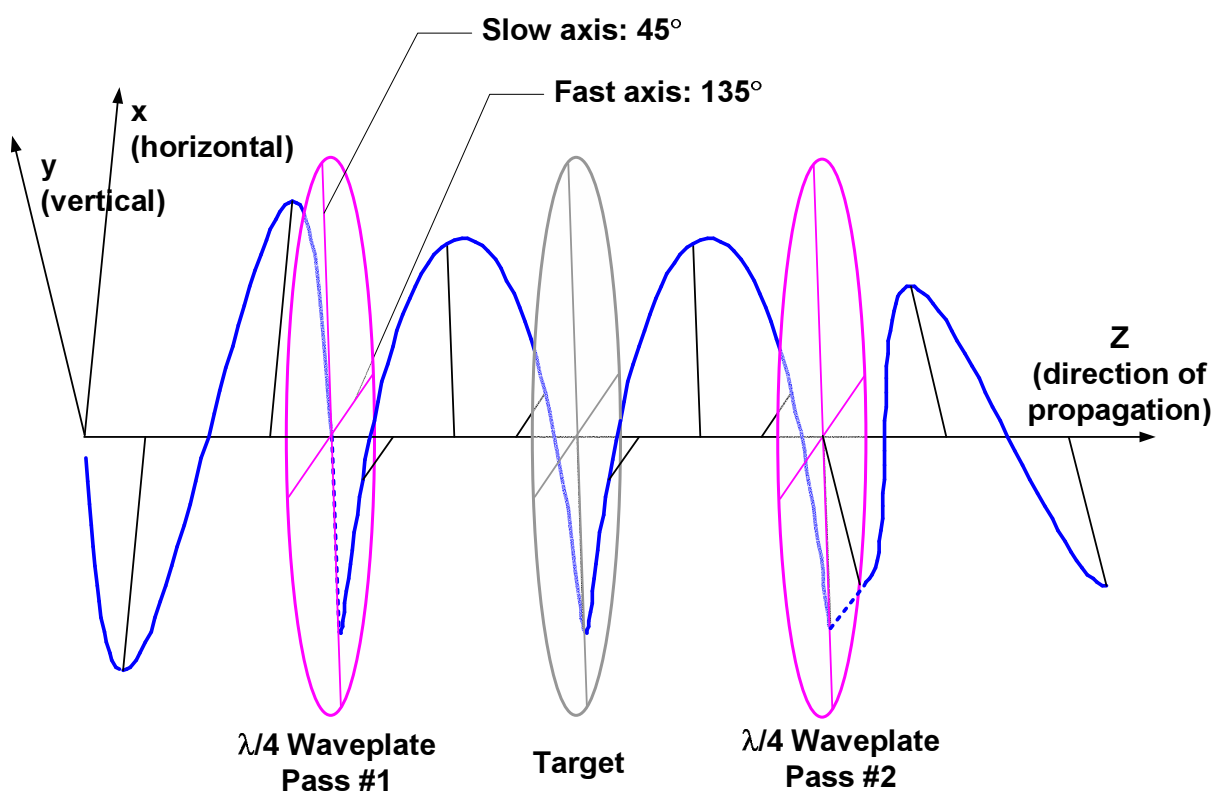
Figure 3.3 Polarization sequence

3. Most of the light passes straight through the 1" PBC, with the remaining light reflecting into a beam dump.

4. The light is converted from horizontal to circular polarization by a $\frac{\lambda}{4}$ waveplate. The waveplate is aligned with its slow axis at a $45°$ angle from horizontal, as shown in Fig. 3.3. In this manner, the transmitted light along the $45°$ diagonal is delayed by $\frac{1}{4}$ cycle with respect to light along the $135°$ diagonal.

5. Light is reflected from the target, but the $90°$ delay between diagonal polarizations is maintained.

6. The second pass through the $\frac{\lambda}{4}$ waveplate converts the light from circular to vertical polarization. After both passes through the waveplate, the $45°$ axis is delayed by $\frac{1}{2}$ cycle with respect to the $135°$ axis.

7. The vertically polarized light reflects from the 1" PBC toward the interferometer section.

Linear polarization can be separated into components according to the rules of complex algebra. For example, the horizontal polarization corresponding to the incident light on the waveplate can be expressed $1 = \frac{1}{\sqrt{2}}\angle 45 - \frac{1}{\sqrt{2}}\angle 135$. The delay of $\frac{1}{2}$ cycle for the light along the $45°$ diagonal is equivalent to a sign change. The resulting expression, $-\frac{1}{\sqrt{2}}\angle 45 - \frac{1}{\sqrt{2}}\angle 135$, represents vertical polarization.

The focal lengths and positions of the cylindrical lenses in the input section are chosen to provide telecentric illumination of the sample and line widths that are as narrow as possible. The use of both telecentric illumination and collection ensures that the incident and reflected angles are as close as possible to the direction of motion, so that these angles need not be taken into account in the Doppler-shift, as discussed earlier. To alleviate diffraction limiting of the line widths, the laser beam is expanded horizontally to a sizable fraction of the relay-to-target numerical aperture.

As shown in Fig. 3.2, the vertically aligned cylindrical lens is placed a distance equal to its focal length from the point of the virtual image aperture. This creates the line-image, which

Table 3.1 Cylindrical lens selection

Stage 2 Mag.	Collimating Lens	Hor. Lens. (f_1)	Vert. Lens (f_2)	Line Size at Image Aperture
1.0	300 mm	100 mm	50 mm	5 mm
0.5	600 mm	50 mm	100 mm	10 mm

is relayed to the target. The horizontally aligned lens is placed with respect to the virtual aperture stop, to achieve telecentric illumination. The focal lengths are set by the line length for the vertical lens and by the numerical aperture for the horizontal lens. Once the target has been brought into focus, the vertical lens is readjusted for the narrowest possible line width. Table 3.1 lists the appropriate cylindrical lenses for the two choices of collimating lens.

3.1.2 Target-to-Table Relay

The table-to-target relay uses the same optics to both illuminate the target and collect light from it. The relay allows the table to be distanced from the experiment by two meters. Another function of this relay is the magnification of the target image to a suitable size for interferometry and image recording. Also, the relay allows for the use of an aperture stop, which prevents vignetting of subsequent optics by limiting the angular aperture.

Fig. 3.4 shows the target-to-table optical relays that were developed to allow studies of particle velocity variation at several length scales. The distance from the input image aperture to the aperture stop was set to 60 mm to obtain telecentric light collection for the single lens configuration. The other configurations are designed to be telecentric by selection of lens power and placement. Fig. 3.4 also shows the path of light rays, with input cones corresponding to the numerical apertures given in Table 3.2. Blue and green lines denote light rays from the center and end of the illuminated line, respectively. It is evident that there should be no vignetting from the relay lenses at the prescribed aperture settings. Note that the configurations which use microscope objectives have an input cone that is limited by the numerical aperture of the objective, while the other configurations are mainly limited by the optics in the interferometer

section. Also, the depth of field decreases with the square of the line length, which is a severe limitation at high magnification. This is a consequence of diffraction limiting[1, 13].

Table 3.2 Acheivable line lengths and associated optical parameters

Stage 1 Mag.	Stage 2 Mag.	Total Mag.	Line Length	Numerical Aperture	Depth of Field	Aperture Diameter
1.33×40x	1.0	53.33	94 μm	0.65	1 μm	1.5 mm
1.33×10x	1.0	13.33	375 μm	0.25	14 μm	2.2 mm
1.33×4x	1.0	5.33	938 μm	0.10	85 μm	2.2 mm
1.33	1.0	1.33	3.75 mm	0.08	0.42 mm	7.2 mm
1.33	0.5	0.67	7.50 mm	0.04	1.7 mm	3.6 mm
0.2	1.0	0.20	25.0 mm	0.012	20 mm	7.2 mm
0.2	0.5	0.10	50.0 mm	0.006	75 mm	3.6 mm

In addition to the magnifications that these relays provide, the experimenter can choose to use the 600 mm collimating lens instead of the 300 mm lens before the interferometer section. This doubles the line length at the sample, but requires changing out the cylindrical lenses according to Table 3.1 and readjusting the adjustable slit. Table 3.2 lists the available configurations and associated optical parameters.

The relays have been designed to have telecentric light collection from the target and have relay length of approximately 2.1 m. They do not use lenses near the center of the relay to simplify lens mounting. To find relay systems which simultaneously meet these requirements, it is suggested to begin with ideal thin lenses in the paraxial approximation ($\sin \theta \approx \theta$). This linear approximation allows the use of matrix optics.

Matrix optics, also referred to as A, B, C, D matrices, is a mapping of optical rays in position and angle from two planes along the optical axis. For a more thorough introduction, please consult the text *Photonics* by Eugene Hecht[10]. The transfer matrix is a mapping of
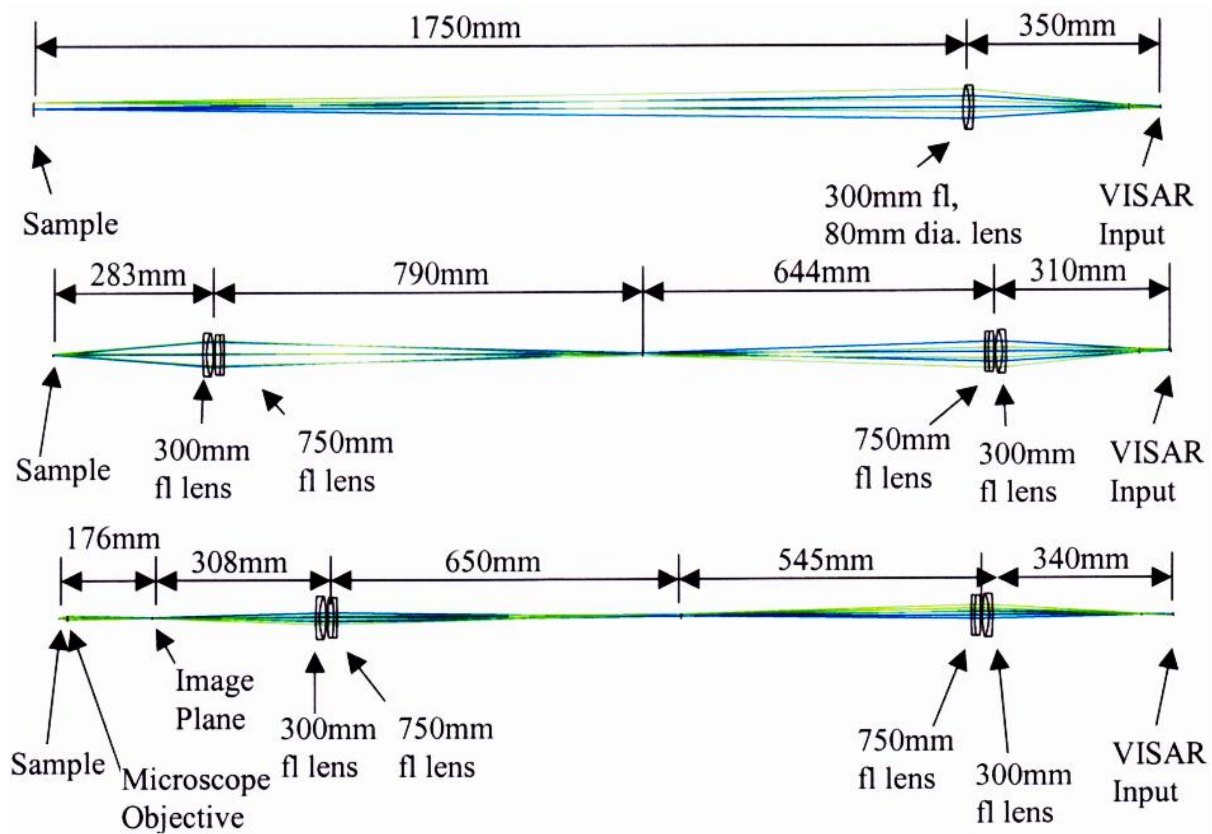
Figure 3.4 Simulated VISAR Table-to-Target Relays: magnification 0.2 (top), magnification 1.33 (middle), magnification 13.3 (bottom). Note: Achromatic lens pairs should always have the more strongly curved sides facing each other.

position–angle pairs and takes on the form:

$$\begin{bmatrix} y_2 \\ \theta_2 \end{bmatrix} = \begin{bmatrix} A & B \\ C & D \end{bmatrix} \begin{bmatrix} y_1 \\ \theta_1 \end{bmatrix} = \mathbf{T_s} \begin{bmatrix} y_1 \\ \theta_1 \end{bmatrix} \tag{3.1}$$

A graphical description of the positions (y) and angles (θ) can be seen in Fig. 3.5.

The transformation matrices for an air-space of length d and for a thin lens of focal length f are as follows:

$$\mathbf{T_{air}} = \begin{bmatrix} 1 & d \\ 0 & 1 \end{bmatrix} \qquad \mathbf{T_{lens}} = \begin{bmatrix} 1 & 0 \\ -1/f & 1 \end{bmatrix} \tag{3.2}$$

Using these we find the transformation $\mathbf{T_x}$, for the example system of Fig. 3.5:

$$\begin{aligned} \mathbf{T_x} &= \begin{bmatrix} 1 & d_2 \\ 0 & 1 \end{bmatrix} \begin{bmatrix} 1 & 0 \\ -1/f_1 & 1 \end{bmatrix} \begin{bmatrix} 1 & d_1 \\ 0 & 1 \end{bmatrix} \\ &= \frac{1}{f_1} \begin{bmatrix} f_1 - d_2 & d_1 f_1 + d_2 f_1 - d_1 d_2 \\ -1 & f_1 - d_1 \end{bmatrix} \end{aligned} \tag{3.3}$$

Common optical constraints can be easily expressed as conditions on the transfer matrix. For example, a focusing system must have y_2 depend on y_1 only, which may be expressed as $\mathbf{T_x}(1,2) = B_x = 0$. Using this condition with Eq. 3.4 we recover the thin lens equation[1], $d_1 d_2 = d_1 f_1 + d_2 f_1$.
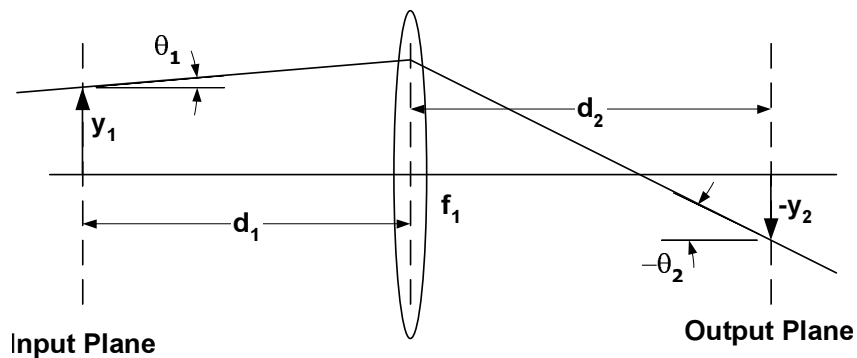
Figure 3.5 Matrix optics example system

As an example of relay design, consider the two-lens relay system shown in Fig. 3.6. The transfer matrix from the target image plane to the plane of the aperture stop is:

$$\mathbf{T_s} = \begin{bmatrix} 1 & d_2 \\ 0 & 1 \end{bmatrix} \begin{bmatrix} 1 & 0 \\ -1/f_2 & 1 \end{bmatrix} \begin{bmatrix} 1 & 2100\text{mm} - d_1 - d_2 \\ 0 & 1 \end{bmatrix} \begin{bmatrix} 1 & 0 \\ -1/f_1 & 1 \end{bmatrix} \begin{bmatrix} 1 & d_1 \\ 0 & 1 \end{bmatrix} \tag{3.4}$$

The transfer matrix from the target image to the input image aperture is then:

$$\mathbf{T}_i = \begin{bmatrix} 1 & 60\text{mm} \\ 0 & 1 \end{bmatrix} \mathbf{T_s} \tag{3.5}$$
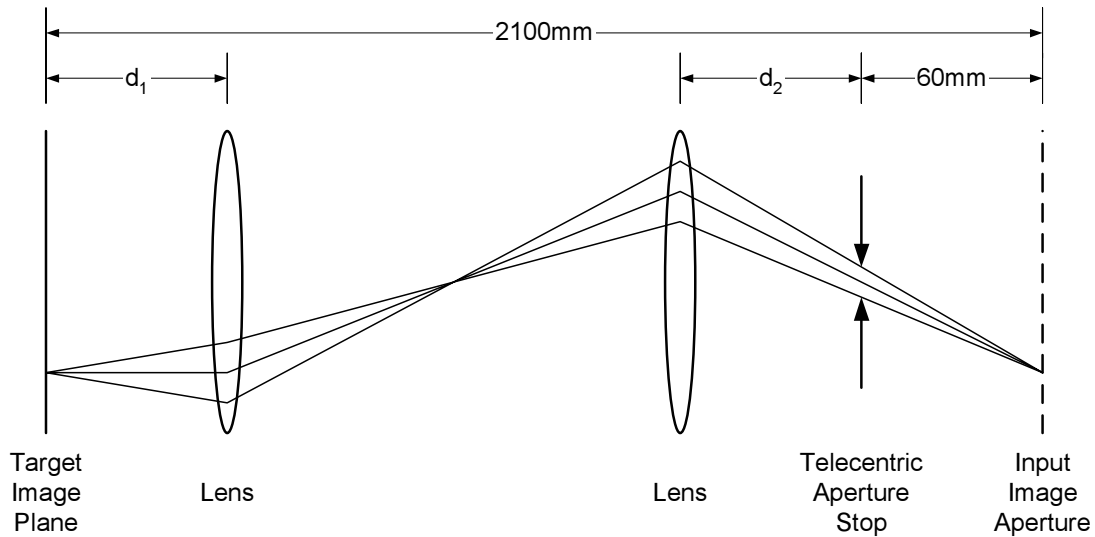
Figure 3.6 Table-to-target relay design

Since the system must image the target to the image aperture, we obtain the first condition: $\mathbf{T_i}(1,2) = B_i = 0$. Next, the requirement for telecentric light collection results in $\mathbf{T_s}(1,1) = A_s = 0$. Another condition is set by the desired magnification, $M = \mathbf{T_s}(1,1) = A_i$. It is convenient to reduce the number of variables by using lenses of equal focal length: $f_1 = f_2$. The design then proceeds as follows:

1. Using symbolic mathematics software, such as MATLAB with the Symbolic Math Toolkit, expand the transfer matrices and solve for d_1, d_2 and $f_1 = f_2$ that satisfy the above conditions.

2. Substitute commercially available achromatic lens pairs for the ideal lenses. Use a pair that have an effective focal length, f_{eff}, which is close to the calculated value.

3. Replace the condition $M = \mathbf{T_s}(1,1) = A_i$ with the condition $f_1 = f_2 = f_{\text{eff}}$, and solve again for d_1, d_2, M. A slightly different magnification should result.

4. Place the lenses into an optical simulation program, such as ZEMAX[14], and refine the lens positions for optimal focus. Check that the system has sufficient resolving power and that the lenses are large enough to avoid vignetting.

When a diffusely reflecting target is used, the interface reflections from the lenses constitute a large fraction of the total reflected light. Additionally, central interfaces of achromatic lens pairs reflect light which comes to a focus near the image aperture. Thus, it is necessary to rotate the target-to-table relay lenses slightly about their vertical axes, so that these reflections do not continue beyond the image aperture. If there is an optical window in front of the target, then it is also necessary to have a small angle between the relay optics and the target.

3.1.3 Interferometer Cavity

The position of the aperture stop functions to keep the light beam close to the optical axis in the interferometer and four-to-one relay sections. Fig. 3.7 shows this part of the optical system. The distance from the optical axis has been exaggerated. Note that within this section, the beam is split apart three times. However, the eight possible paths are optically equivalent and can be considered as a single optical axis.

The beam of light under consideration is from a point at the extreme end of the line at the target. By design, the beam crosses the optical axis again at the final PBC. This makes the alignment of the four-to-one relay less demanding and requires less area of the final focusing lens. Each of the four output beams is limited to one-half of the final lens due to the right-angle-reflector.
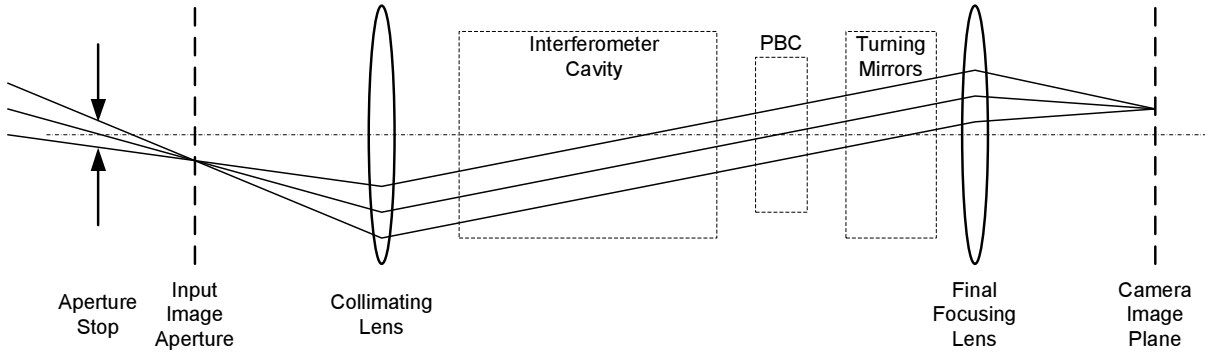
Figure 3.7 Optical view of interferometer section

3.1.4   Four-to-one Relay to Camera

Fig. 3.8 shows a simplified schematic of the four-to-one optical relay that routes the light from the interferometer to the streak camera. The light in the interferometer and relay sections is collimated. This creates a mapping from positions at the camera image plane to angles within the optical relay. The form of this mapping is:

$$
\begin{bmatrix} x_1 \\ x_2 \\ x_3 \\ x_4 \end{bmatrix} = c \begin{bmatrix} -1 & 0 & 1 & 0 \\ 1 & 0 & 0 & 1 \\ 0 & -1 & 1 & 0 \\ 0 & 1 & 0 & 1 \end{bmatrix} \begin{bmatrix} \phi_1 \\ \phi_2 \\ \phi_3 \\ \phi_4 \end{bmatrix} \tag{3.6}
$$

where ϕ_i is the rotation of turning mirror $\mathbf{M_i}$, with $i = 1, 2, 3, 4$. x_i represents the resulting displacement of the ith image. The numbers 1, 2, 3 and 4 correspond to the $\sin$, $\cos$, $-\cos$ and $-\sin$ images of Fig. 3.8, respectively. The mapping is identical for both axes of the image plane.

The matrix in Eq. 3.6 is singular and thus the arrangement of the quadrature images at the camera input is limited. One possible arrangement is with the image offsets along an equally spaced line. This arrangement is well suited for line-VISAR. Another possibility is to place the images in a 2×2 rectangular array. This configuration would be optimal for resolving velocity in two spatial dimensions with a framing camera.

Streak Camera

M$_3$ (**sin**, **cos**)

M$_4$ (**-sin**, **-cos**)

Turning Mirrors

Polarizing Beamsplitter Cube

(**-sin**, **cos**)

M$_1$

(**sin**, **-cos**)

M$_2$

Laser

Delay Etalon

Sample

λ/8 Waveplate

sin

cos

-cos

-sin

Δx$_2$

Δx$_1$

Streak Direction
(time axis)

Image at streak camera input face

Legend:
Horizontally Polarized Light
Vertically Polarized Light
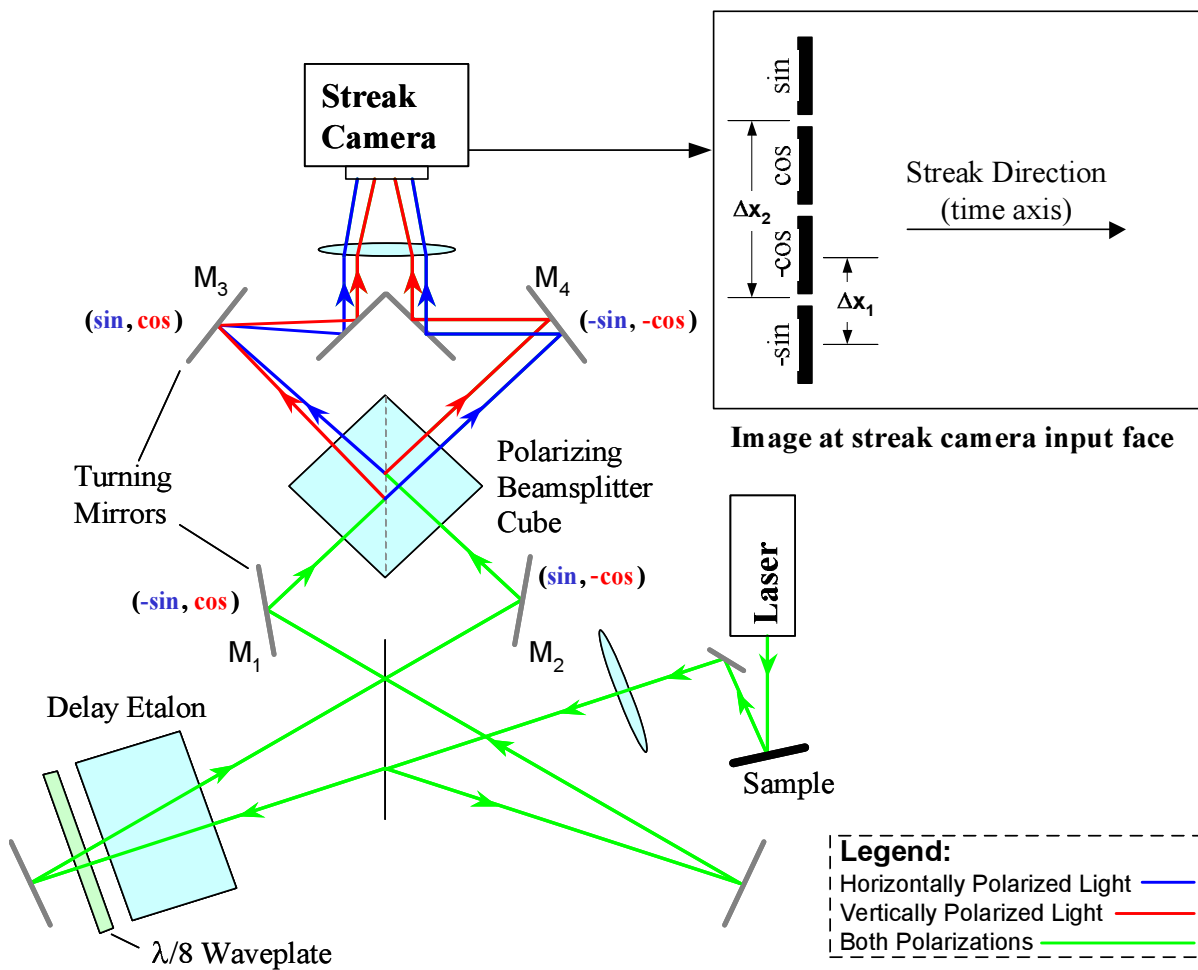Both Polarizations

Figure 3.8 Four-to-one relay to camera

In practice, the separation of the images is done by tweaking with the turning mirrors and observing the effect using the setup camera in continuous-capture mode. Referring to Fig. 3.8, it is best to perform the minor separation (Δx_1) by turning mirrors M_1 and M_2, and perform the major separation (Δx_2) with mirrors M_3 and M_4. This will minimize the beam displacements. The order of the quadrature images is not critical. If the order is reversed, the analyzed phase will simply be negated, and the analysis software has an option to negate the phase.

3.2   Alignment Procedure

Occasionally, the optics of the line-VISAR table should be realigned to prevent vignetting. Particular care is needed with the four-to-one optical relay, since different amounts of vignetting between quadrature images may lead to a systematic, position-dependent velocity error. The following alignment procedure was developed to minimize this problem.

1. Remove all lenses except the final focusing lens. This includes the cylindrical optics and the beam expanding telescope.

2. Turn the flipping mirror toward the setup camera and turn the setup camera on in continuous-capture mode. Turn the laser on with the minimum power setting and set the acousto-optic modulator to 1% duty cycle. Increase laser power until is is possible to see the scattered light from mirrors after the first iris.

3. Check that the laser beam is at a constant height and is centered over the table screw-holes up to the 1" PBC. A pair of alignment stands were made to help with this.

4. Replace the target relay with a mirror. Align the mirror so that it reflects directly back onto the same spot on the previous turning mirrors. It will be necessary to rotate the $\frac{\lambda}{4}$ waveplate to see this reflection.

5. Rotate the $\frac{\lambda}{4}$ waveplate to minimize the amount of reflected light which continues straight through the 1" PBC and back toward the laser.

6. Align the optics from the 1" PBC to the final lens so that the beam is at the correct height and properly centered, and the optics are centered with respect to the beam. The etalon elements should be parallel with the first pass of the beam and approximately $5°$ from the second pass. This prevents glass interface reflections from reaching the camera.

7. Center the aperture stop and input image aperture with respect to the beam.

8. Translate the final focusing lens until the spot size at the setup camera is minimized. Reduce laser power or add neutral-density filters if the image begins to saturate.

9. Turn the mirrors of the four-to-one relay to arrange the four dots in an equally-spaced line. Remember to use the mirrors closest to the camera to perform the major separation.

10. Check that the beam is still centered on the optics of the relay.

11. Reinsert the collimating lens between the input and interferometer sections.

12. Turn off the laser. Using an incandescent light, such as a desk lamp with a magnetic base, reflect light off the surface of the adjustable slit so that it will be visible through the system at the setup camera. Move the collimating lens to obtain the best focus at the setup camera. Scratches on the surface of the metal will be visible.

13. Eliminate the rotation caused by the periscope mirrors. A convenient way to do this is to use an application window such as *Notepad* as a straight-edge in front of the video capture application, as shown in Fig. 3.9. Adjust the periscope mirrors until the edges of the slit aperture are parallel to the application window.

14. Adjust the slit size and finalize the positions of the quadrature images. Note that the active area of the setup camera is 7.7 mm x 6.1 mm, while the Imacon 790 streak camera has a 10 mm wide input.

15. If the relative positions of the setup and streak camera are suspected to have moved, use the incandescent light method to find the position of the streak camera that gives the best focus.
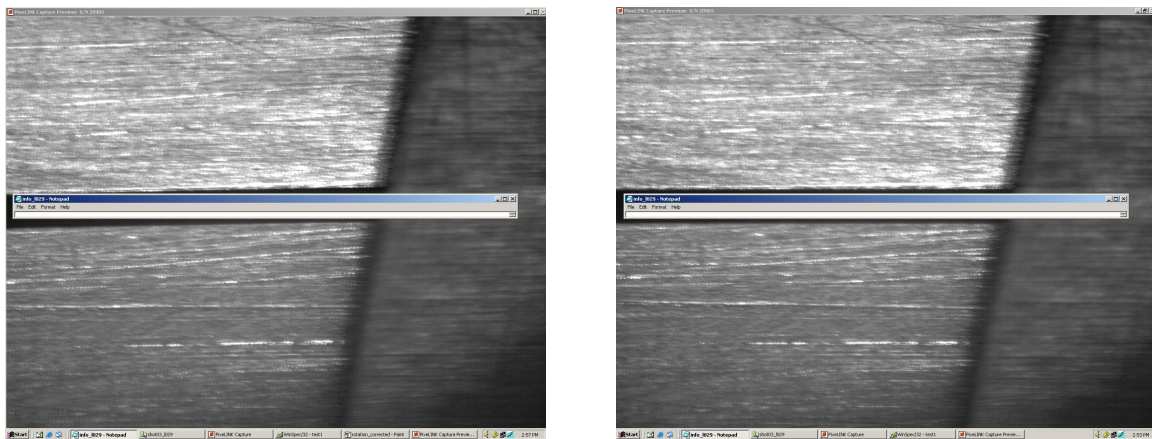
Figure 3.9 Image rotation caused by the periscope mirrors. Poor rotation aligment is shown at left; good alignment shown at right.

3.3   White-Light Interference

The optimal interferometer mirror positions may be found to within a few tenths of a mil-limeter by simply searching for the center of the "bull's eye" pattern using the setup camera. When a diffuse reflector is used, the spatial coherence of the reflected light is small, and thus the recombined images from the interferometer must overlap precisely to obtain interference. When the mirrors are not positioned optimally, the best fringe contrast will coincide with a "fringe comb" pattern (Fig. 3.10(b)). The goal here is to have maximum contrast coincide with a full-field fringe pattern. That is, each of the quadrature images interferes with a constant phase, and the entire image becomes light dark at the same instant.

(a)

(b)

(c)

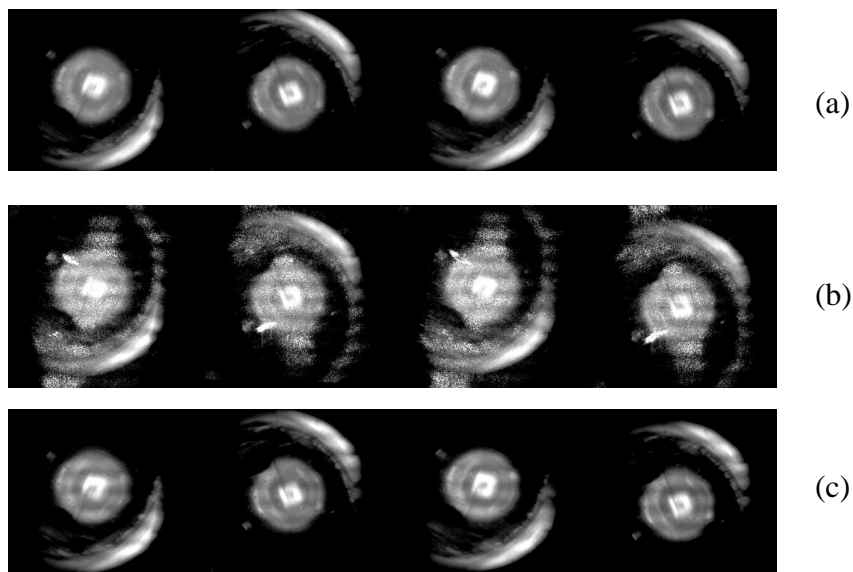Figure 3.10 Setup camera pictures: (a) LED imaged but not interfered, (b) using laser reflection to aid alignment, (c) LED-only interference

White-light interference allows the mirrors to be positioned to an accuracy of about $10\,\mu$m. However, the user must overcome the limited spatial and temporal coherence of the light to obtain interference fringes. With good technique and practice, this should be possible in about 30 minutes.

When finding white-light fringes, the etalons are removed, but the waveplate and main beamsplitter remain as delay elements. Thus when the mirrors are positioned for optical equivalence (full-field fringes), there is a transit time difference between the two interferometer legs. The beamsplitter has a thickness of 0.375 inches and is made of BK7 with an index of refraction n=1.5195 at the Verdi wavelength (532 nm). The waveplate has a thickness of 0.050 inches and an index of n=1.52. The transit time difference at optical equivalence is then given according to Chapter 2:

$$c\tau \ = \ \sum_{i=1}^{N} L_i \left(n_i - \frac{1}{n_i} \right) \tag{3.7}$$

$$= \ 2 \left(0.375\text{in} \left(1.5195 - \frac{1}{1.5195} \right) + 0.050\text{in} \left(1.55 - \frac{1}{1.55} \right) \right) \tag{3.8}$$

$$= \ 0.737\text{in} = 18.708\text{mm} \tag{3.9}$$

The motorized beamsplitter is on a translation stage that is oriented parallel to the incident light beam and $5°$ from reflected beam. Fig. 3.11 shows the effect of translating this mirror toward the main beamsplitter. The resulting change in transit time is given according to:

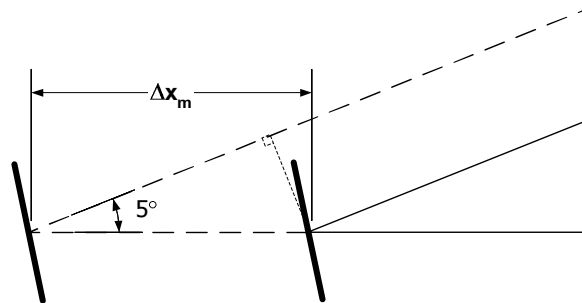$$c\Delta\tau = (1 + \cos(5°)) \Delta x = 1.9962\Delta x \tag{3.10}$$

Figure 3.11 Moving the motorized mirror to decrease time delay

Using Eq. 3.9 and Eq. 3.10, we find that a mirror translation of Δx_{m0}=9.372 mm toward the beamsplitter brings the interferometer legs from optical equivalence to temporal equivalence. Temporal equivalence implies that the transit time difference is zero, a necessary condition for

white light interference. Having this distance in hand greatly speeds the search for white light fringes. The following procedure was used to obtain white-light interference:

1. Remove all delay elements except the $\frac{\lambda}{8}$ waveplate and main beamsplitter.

2. Place the white-light interference LED (Fig. 3.20) at the target location. Plug in the LED and bring the emitting element into focus at the setup camera (Fig. 3.10(a)).

3. Turn on the Verdi laser. Increase the power until the laser light reflected from the LED is visible with the setup camera.

4. Using the translation stage that supports the motorized interferometer mirror, move and tilt the mirror to obtain an optimal full-field fringe pattern, as described above.

5. Move the translation stage toward the main beamsplitter by a distance of Δx_{m0}. This accounts for the transit time difference caused by the $\frac{\lambda}{8}$ waveplate and main beamsplitter.

6. Adjust the angle of the motorized mirror until maximum contrast is observed in the interference fringes of the reflected laser light. The setup camera display should become similar to Fig. 3.10(b). The laser light has very long temporal coherence, but its spatial coherence is similar to the LED after a dispersive reflection. This step takes advantage of the laser's long temporal coherence but limited spatial coherence to precisely align the images. Without using the laser in this step, it is very difficult to find the correct mirror position and alignment that corresponds simultaneously to spatial and temporal coherence of the LED light.

7. Turn off the laser and look for evidence of interference from the LED light. Fig. 3.10(c) shows an example of white-light interference. If interference is not seen, translate the mirror in increments of about 20 μm, and stop to look for interference after each step. If it is necessary to translate by more than 500 μm, use reflected laser light to realign the images.

Etalon Length	$c\tau$(mm)	τ(ns)	Δx_m(mm)
0.0"=0 mm	18.708	0.0624	9.372
0.4"=10.16 mm	36.211	0.1208	12.845
0.8"=20.32 mm	53.715	0.1792	16.319
1.6"=40.64 mm	88.721	0.2959	23.266
3.2"=81.28 mm	158.735	0.5295	37.160
6.4"=162.56 mm	298.763	0.9966	64.949
9.6"=243.84 mm	438.790	1.4637	92.738

Table 3.3 Etalons with associated time constant and mirror translations

8. At the first evidence of white-light interference, maximize the contrast by adjusting mirror angle as well as translation. When the contrast in near optimal, record the position reading of the translation stage.

After the white-light interference fringes are found, the etalons may be re-inserted. The motorized mirror is moved away from the beamsplitter by the distance:

$$\Delta x_m = \Delta x_{m0} + \sum_{i=1}^{N} L_i \left(1 - \frac{1}{n_i} \right) \tag{3.11}$$

Δx_m is the distance the mirror must be translated to go from white-light interference with no etalons to optical equivalence with a given set of etalons. Here, N is the number of etalons, L_i are the etalon lengths, and n_i are the corresponding refractive indices. With the WSU line-VISAR system, BK7 etalon with thicknesses of 0.4, 0.8, 1.6, 3.2 and 6.4 inches are available. These provide 32 choices for total delay, of which Table 3.3 shows a select few. Also listed are the associated values for τ and Δx_m, which include the delay effects of the beamsplitter and waveplate.

3.4   Instrument Preparation and Timing

To find the actual magnification of the target, a metal scale was held at the target location. An assistant captured the image on the setup camera when it came into focus. An example is shown in Fig. 3.12. The minor spacing on the scale is 0.2 mm.
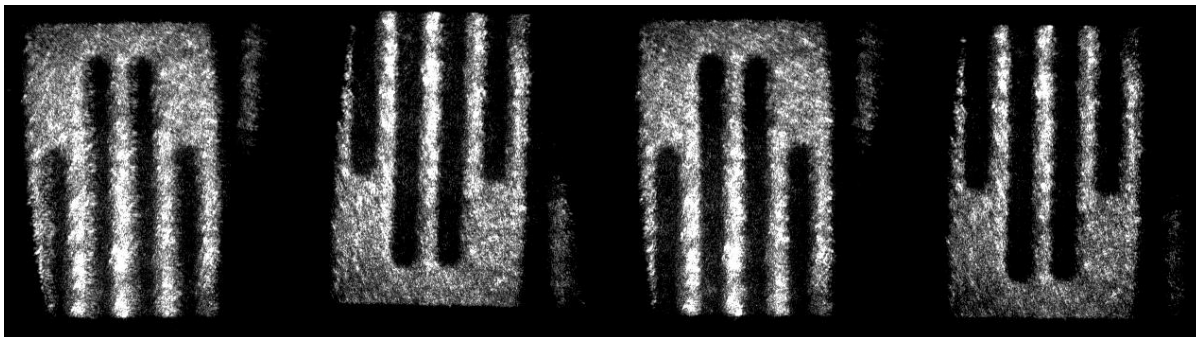

Figure 3.12 A metal scale at the target location

The generation of a timing signal to trigger the streak camera requires some attention. There is some delay from the timing signal to the visible part of the streak. To aid in determining this delay, a simple timing LED (Fig. 3.20) was assembled. This LED can be connected directly to the delay generator, but limited light output requires that the LED be placed directly against the streak camera input. Using this technique, the delay from the triggering of the streak camera to the center of the streak was found to be 3.5, 2.2, 1.0 and 0.6 μs for streak rate settings of 100, 50, 20 and 10 ns/mm. The accuracy of this method is limited to 10-20% of the total time window because the entire input of the streak camera is illuminated.

With the gas gun experiments, contact-trigger pins were used to create a reference timing signal. Simple calculation of the pin heights and projectile velocity gave accurate estimates for impact time.

Contact-trigger pins are not available for the laser-driven flyer apparatus. Instead, a timing signal is produced by the drive-laser system. Using this signal, a highly-accurate technique was discovered to synchronize the streak record to the launch event. A target cell was inserted containing only a 1 mm thick piece of teflon tape. When pulses from the drive laser hit the

Streak Rate	20 ns/mm
Total Time Window	0.8 μs
Trigger Delays:	
AOM on	16.4 μs
Streak camera	18.4 μs
AOM off	23.4 μs
Delay	5 s

Table 3.4 Timing parameters – laser flyer

tape, a plasma emission occurred that was very localized in time and easily visible on the streak record. Using this method, the time from the trigger signal to the pulse arriving at the target cell was found to be 18.9 μs.

When using the laser-driven flyer, the teflon-tape timing method decribed above was used to set the location of the launch event in the streak record. Then, the Verdi laser was turned on and streaks were taken to ensure that the acousto-optic modulator turned on a few microseconds before the streak and that it remained on until the end of the record. An unused output of the delay generator is set to a delay of 5 s to prevent repeated triggering. The resulting trigger time delays are shown in Table 3.4

3.5   Specific Experiments

This section presents experimental details that are unique to the three experiments that will be considered in this thesis.

3.5.1   Laser-Driven Flyer Launch

A simplified schematic of the laser-driven flyer target cell is shown in Fig. 3.13. A photo of the target cell is shown at the end of the chapter in Fig. 3.21. The drive laser ablates some material from the flyer, accelerating it toward the rear window. Air in the target cell is evacuated before the experiment. The flyer contacts and splinters the rear window after about 500 ns, after

accelerating to a velocity of around 1 km/s. The rear window generally stays intact, protecting any other nearby optics.
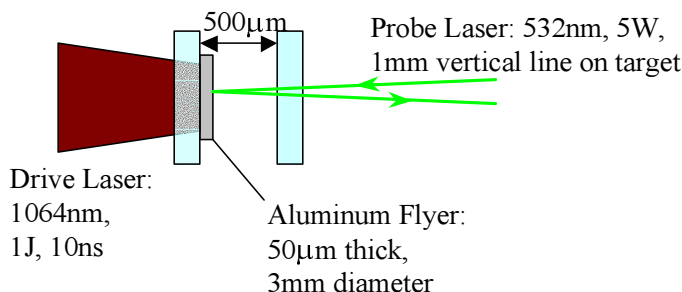

Figure 3.13 Laser-driven flyer schematic

3.5.2   Conventional Projectile Impacts

Two experiments were performed with the 4-inch diameter gas gun. The gun chamber is about two inches higher than the laser-driven flyer target cell. Since the line-VISAR table could not be raised by that distance, the table legs were put onto custom teflon blocks. These blocks, which are visible in Fig. 3.22, have a circular recess so they will not slip out from the table legs. In addition, a simple frame is shown which supports a tent of black fabric. In conjunction with a neatly sized cardboard box around the streak camera input, the ambient light level incident on the streak camera was reduced. Although the laser light level is much more intense than the room light, these precautions reduce the wear on the streak camera while waiting for the shot.

The first experiment using a gas gun involved a fused silica symmetric impact. A simplified schematic of this experiment is shown in Fig. 3.14. The desired projectile velocity was 600 m/s. Fused silica was chosen because it supports this relatively high impact velocity without forming a shock-wave[15]. This results in a velocity profile that increases in a smooth ramp. This shot will be compared to previous point-VISAR data taken by Kurt Zimmerman[16].

The second experiment involved a symmetric impact of aluminum (Fig. 3.15). The desired velocity in this case was 409 m/s for comparison with previous point-VISAR data taken by the author. In this case, a shock-wave does occur, resulting in a near-discontinuity of the velocity record. The limited time resolution of the line-VISAR will require inserting a fringe, or jump,
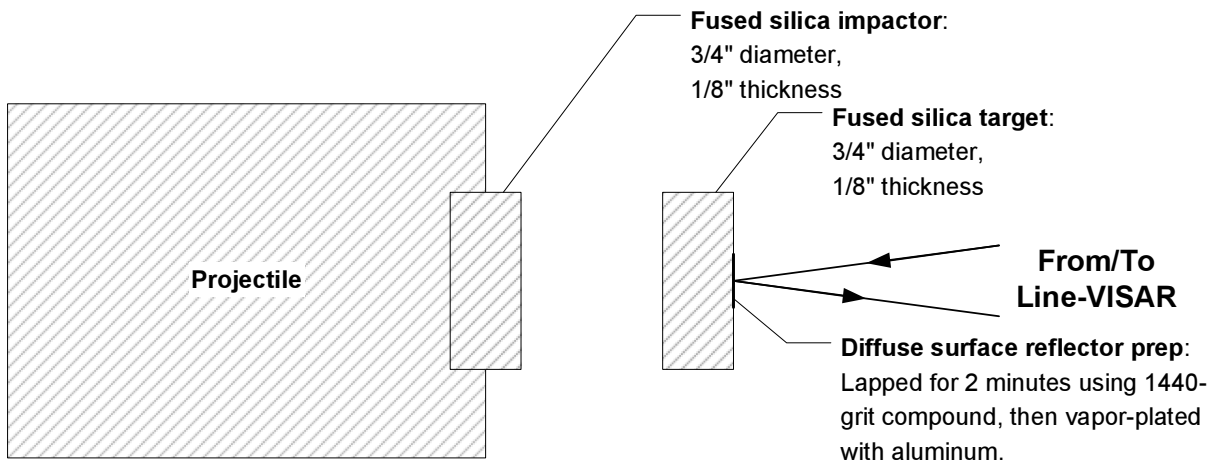
Fused silica impactor:
3/4" diameter,
1/8" thickness

Fused silica target:
3/4" diameter,
1/8" thickness

Projectile

**From/To
Line-VISAR**

Diffuse surface reflector prep:
Lapped for 2 minutes using 1440-
grit compound, then vapor-plated
with aluminum.

Figure 3.14 Fused silica symmetric impact with gas gun

1mm gap to allow
for spall in target

Aluminum impactor:
3/4" diameter,
1/16" thickness

Aluminum target:
3/4" diameter,
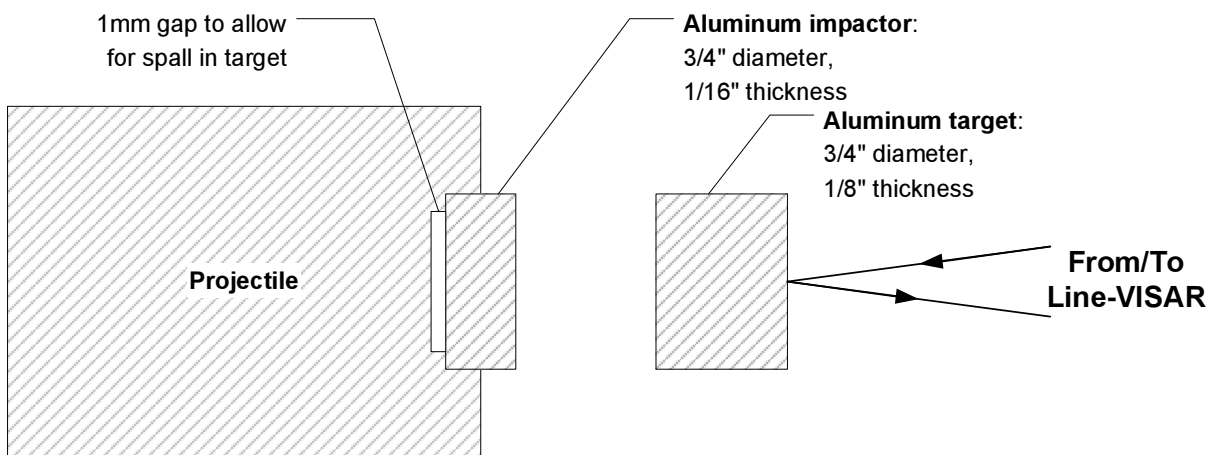1/8" thickness

Projectile

**From/To
Line-VISAR**

Figure 3.15 Aluminum symetric impact with gas gun

at the shock transition. In the shocked state, a variation in the particle velocity with respect to position is expected to be observable, due to the interaction of the shock-wave with aluminum grain boundaries. This effect should be exaggerated by spall, which is the formation of voids within the material.

To produce spall, the impactor thickness is set to half the thickness of the target. Fig. 3.16 shows an x-t diagram for this experiment. In the diagram, compressive shock waves are denoted with an S and rarefactions are denoted with an R. As shown, this experimental arrangement leads to the intersection of a forward and reverse traveling rarefaction wave near the center of the target. The combined effect of the rarefactions places the material under a uni-axial tension greater than aluminum can support. The aluminum separates at a spall plane at this location. The VISAR-facing section of the target then behaves independently, supporting a reverberating shock wave.
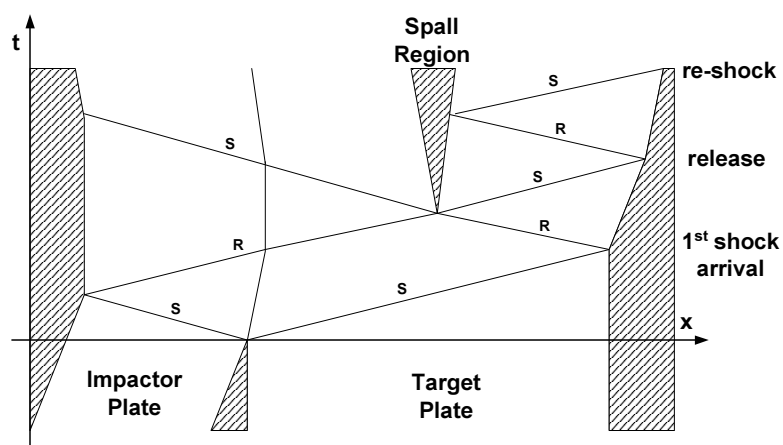

Figure 3.16 x-t diagram showing spall generation

3.6   Photos From Experiments

Figs. 3.17 and 3.18 show the WSU line-VISAR in preparation for experiments with the laser-driven flyer apparatus. The target cell can be seen in Fig. 3.18. Its location is at the intersection of the two longest optical rails just to the right of the photo center.

Fig. 3.19 shows close-up views of the input optical section and four-to-one relay system. Useful timing and alignment equipment referred to in this chapter are shown in Fig. 3.19. Fig. 3.20 shows three items that are useful for aligning the line-VISAR, which are mentioned in the alignment procedure above.

Fig. 3.21 contains photos of the laser-driven flyer cell and the left leg of the interferometer. The motorized mirror and remote control are visible. Fig. 3.22 shows the line-VISAR in preparation for an experiment using the four-inch gas gun.

Fig. 3.23 shows the LED used for white-light interference, mounted inside the 4-inch gun target chamber. The LED is at the far right of the picture, at the same distance as the target. The final mirror, which is mounted on a gray plastic break-away mount, is moved out of the light path. Fig. 3.24 shows the lenses exposed but otherwise ready for the experiment. Finally, Fig. 3.25 shows the complete cover that was used to protect the relay lenses.
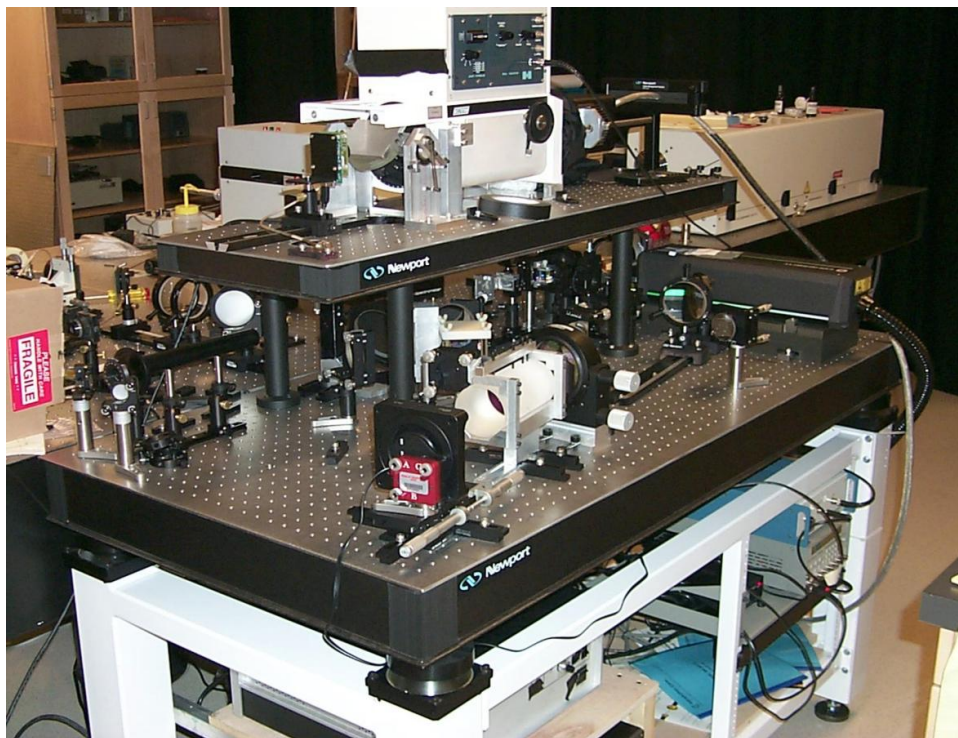
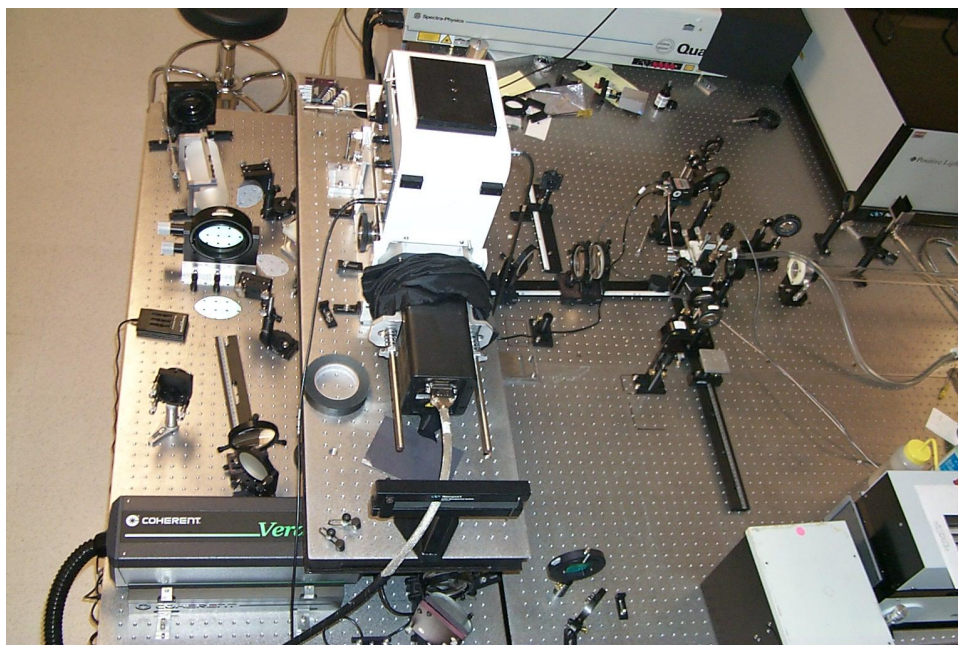Figure 3.17 WSU line-VISAR system

Figure 3.18 Bird's eye view of line-VISAR in preparation for experiments with laser-driven flyer
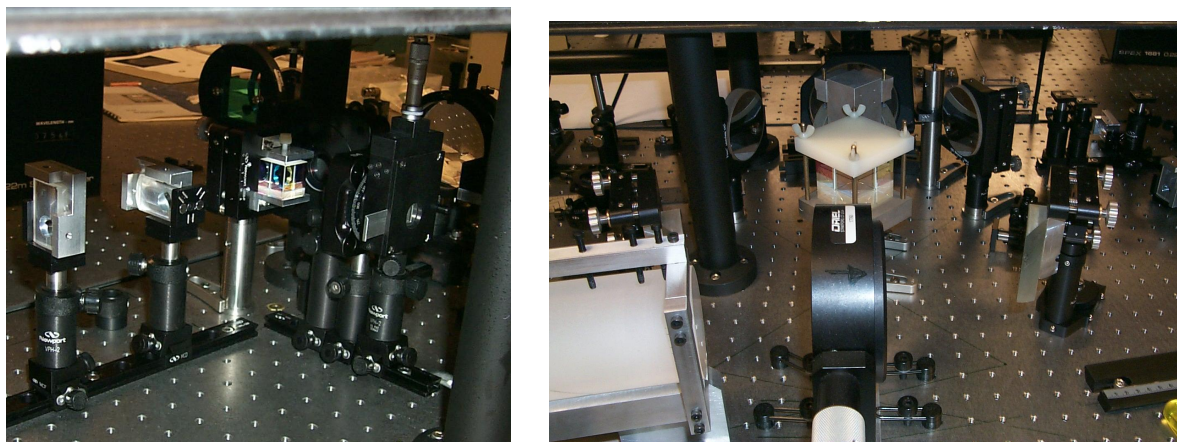
Figure 3.19 Input optics section (left), novel four-to-one relay system (right)
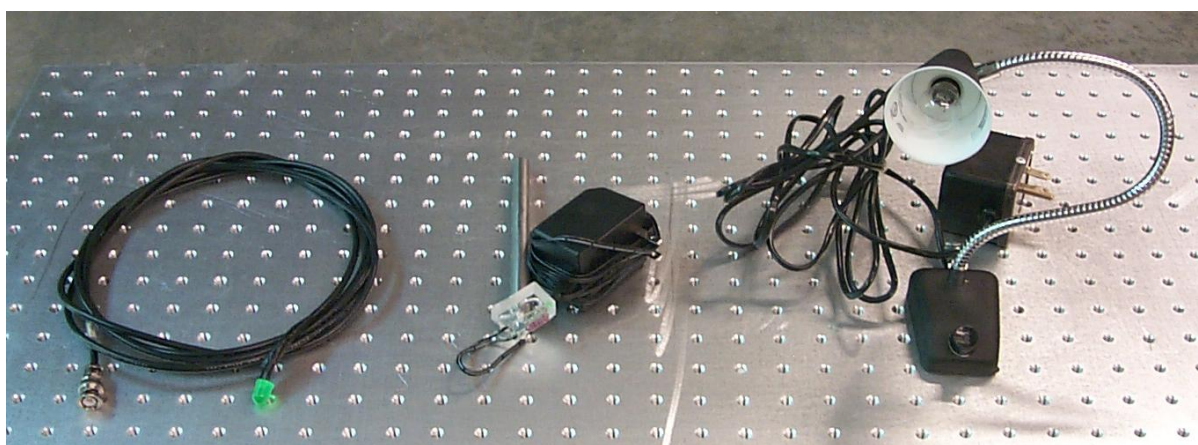
Figure 3.20 Setup equipment: timing LED (right), white-light interference LED with power supply (center), desk-lamp with magnetic base (left)

Figure 3.21 Laser-driven flyer target cell (left), motorized interferometer mirror (right)

Figure 3.22 Line-VISAR in preparation for experiments with gas gun

Figure 3.23 LED for white-light interference at target

Figure 3.24 Gas gun chamber with relay lenses exposed

Figure 3.25 Gas gun chamber with relay lenses protected

Chapter 4

Experimental Results and Analysis

4.1 Problem of Specular Targets and Angular Dependence
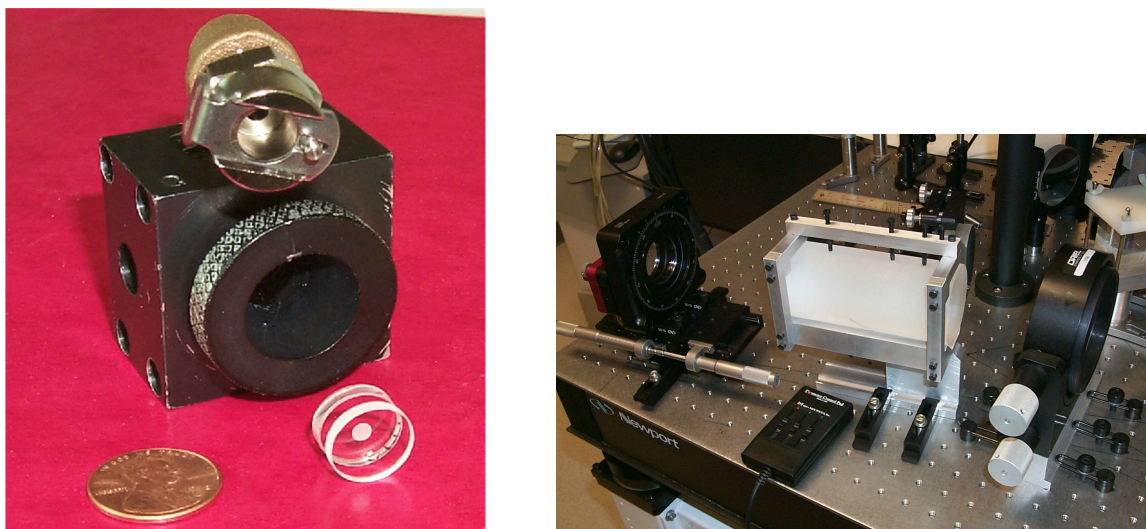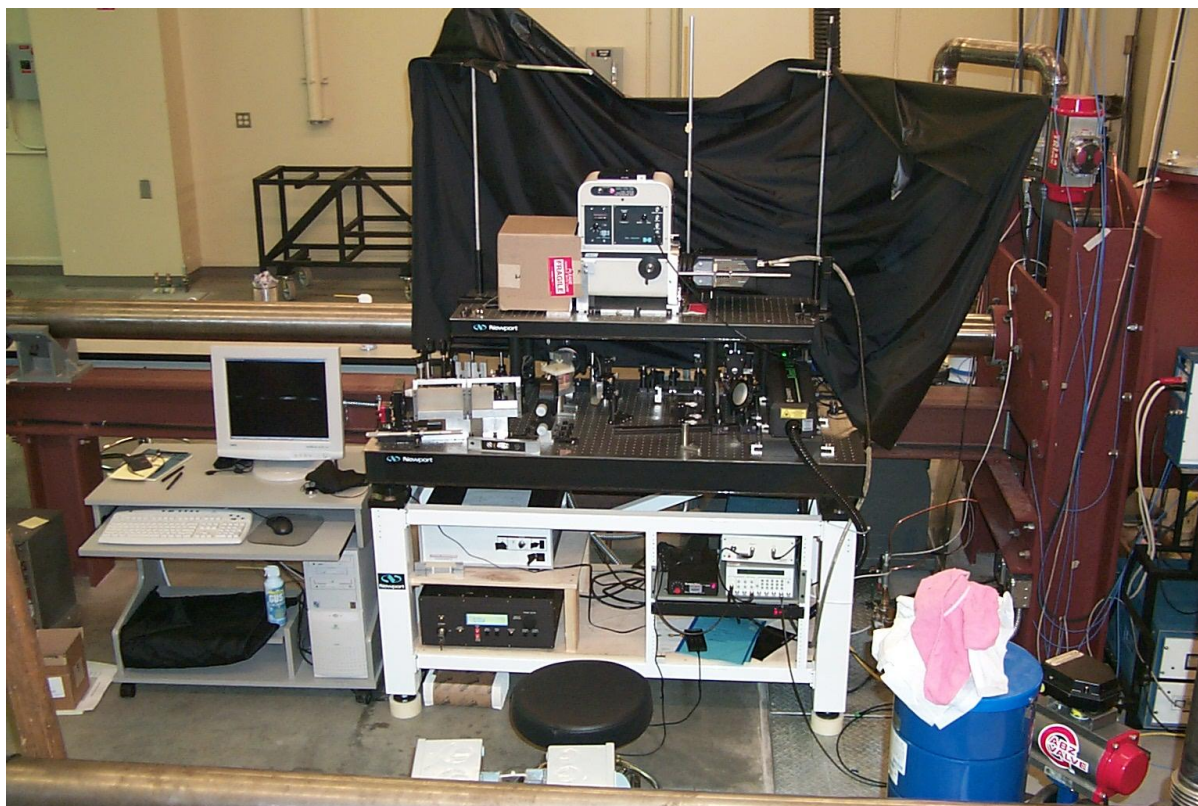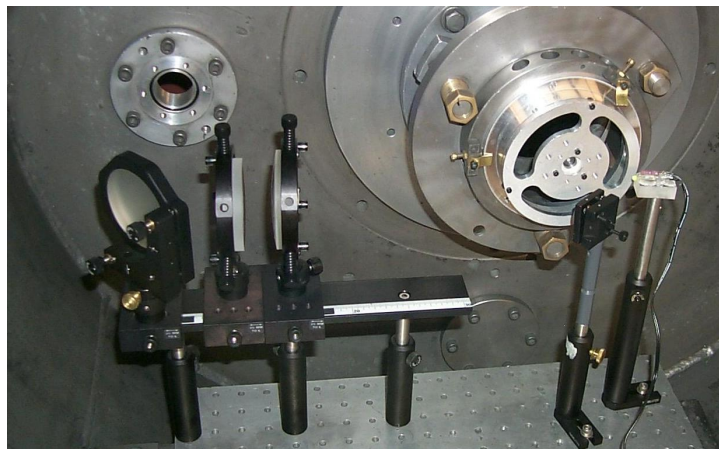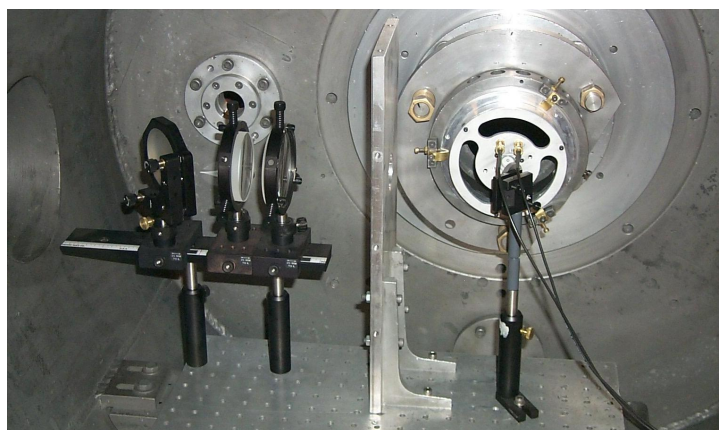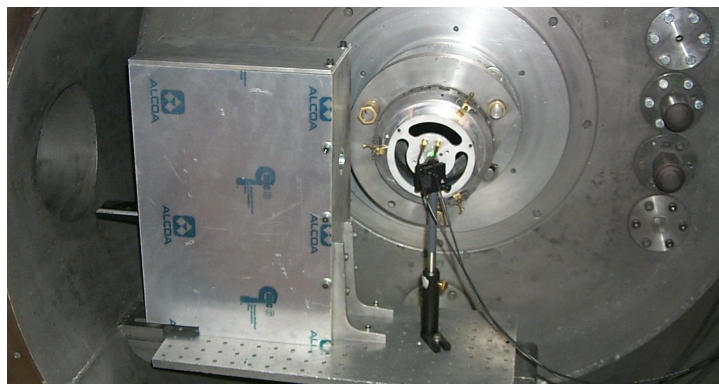
The laser driven flyer apparatus was an indispensable tool to the development of the WSU line-VISAR system. This small-scale shock-wave generator offers quick turn-around time between shots, simple target preparation, and cleanliness. These characteristics were invaluable in discovering and alleviating the problems encountered with the use of specular targets.

Specular targets are commonly used in VISAR studies because they allow high light collection efficiency. However, it was eventually discovered that the fringe pattern depended on the angle of the target. This was first observed by applying a small torque to a loosened laser-flyer target-cell and observing the fringe pattern on the setup camera. Further evidence of this dependence is shown in Fig. 4.1, which shows a mirror at the target with several visible scratches. Note that the indicated smaller scratch appears to be out of phase with the mirror surface surrounding it. This is evident from the scratch area being noticeably brighter than its surroundings in the $-\sin$ image and noticeably darker in the $\sin$ image. This angular dependence may be present in fringe-displacement line-VISARs, but it would be more difficult to discover it by similar tests. Fringe-displacement line-VISAR is much less sensitive to localized fringe shifts compared to push-pull line-VISAR.

Fig. 4.2 shows a typical raw image from the launch of a specularly-reflecting laser-driven-flyer. Note the bright bands which appear after launch and are similar across the four quadrature streak images. These large intensity fluctuations greatly hinder accurate velocity analysis.
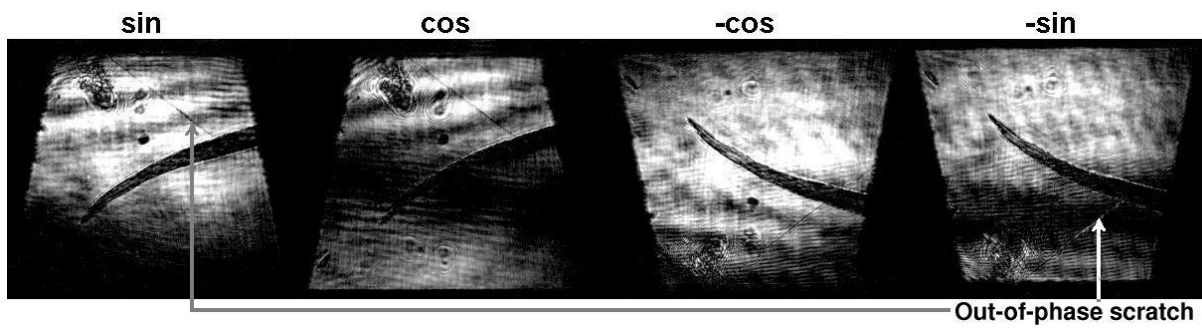
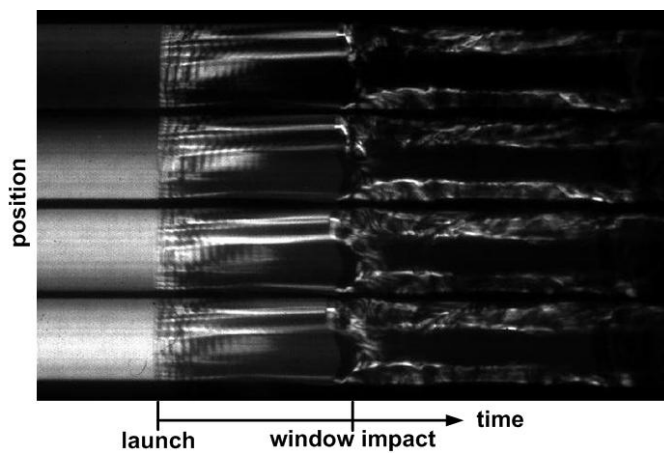Figure 4.1 Scratched mirror target

Figure 4.2 Raw data, specularly reflecting laser-driven flyer

Later experiments showed that the shape of the flyer changed significantly during launch, which may induce vignetting and lead to these strange features.

Despite the increased laser power requirement, all of the remaining experiments used diffusely reflecting targets. Also, note that the raw images for the remaining shots (Figs. 4.3, 4.5, 4.6) have a different characteristic banding both before and after the launch/impact event. This is a result of laser speckle, a consequence of diffuse reflectors. Laser speckle is a mixed blessing for the line-VISAR; it provides a pattern to align the quadrature images in position, yet any misalignment leads to a ripple effect in the velocity record. This effect currently sets the lower limit for the measurement of velocity variations in position, which is about 2–4 m/s.

4.2 Results from Diffusely Reflecting Laser-Driven Flyers

A very simple change led to successful recording of laser-driven flyer launches: the flyers were turned over! The flyers are produced by chemically etching disks out of a sheet of aluminum. As a side effect of this process, one side of the aluminum became slightly pitted and diffuse. Normally this "inferior" side is glued to a glass window so that it will face the drive laser. Facing this side toward the line-VISAR led to much more useful recordings.

Fig. 4.3 shows one of the first successful recordings performed with the WSU line-VISAR. The launch begins at the left of the image and the flyer impacts the glass rear window at the right. By inspection of the raw quadrature images, the flyer appears to strike the rear window with the edges first and center last. Indeed, the computed velocity profile, Fig. 4.4, shows that the center of the flyer accelerates more slowly than the edges. Another feature observed in the velocity profile is a decaying ripple of velocity with time. This feature is also observed in point-VISAR records of the flyer launch. It is a result of the shock-wave reverberating through the thin flyer.
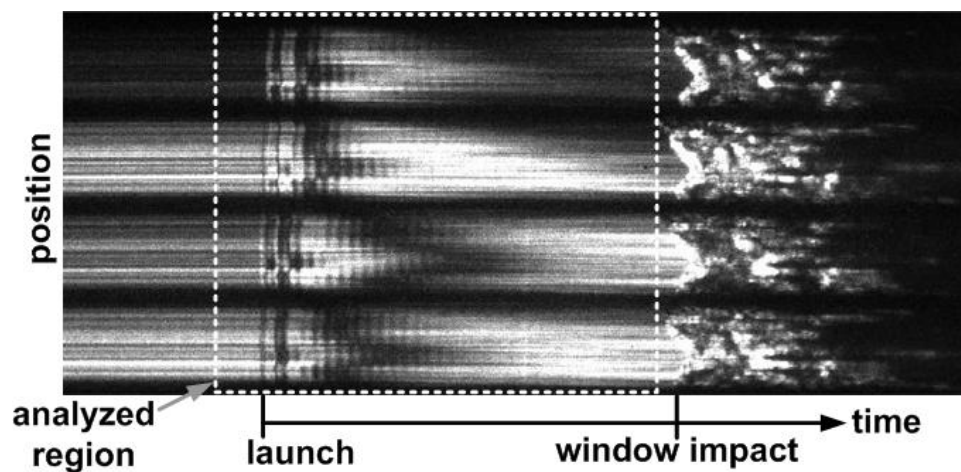
Figure 4.3 Raw streak image, laser-driven flyer
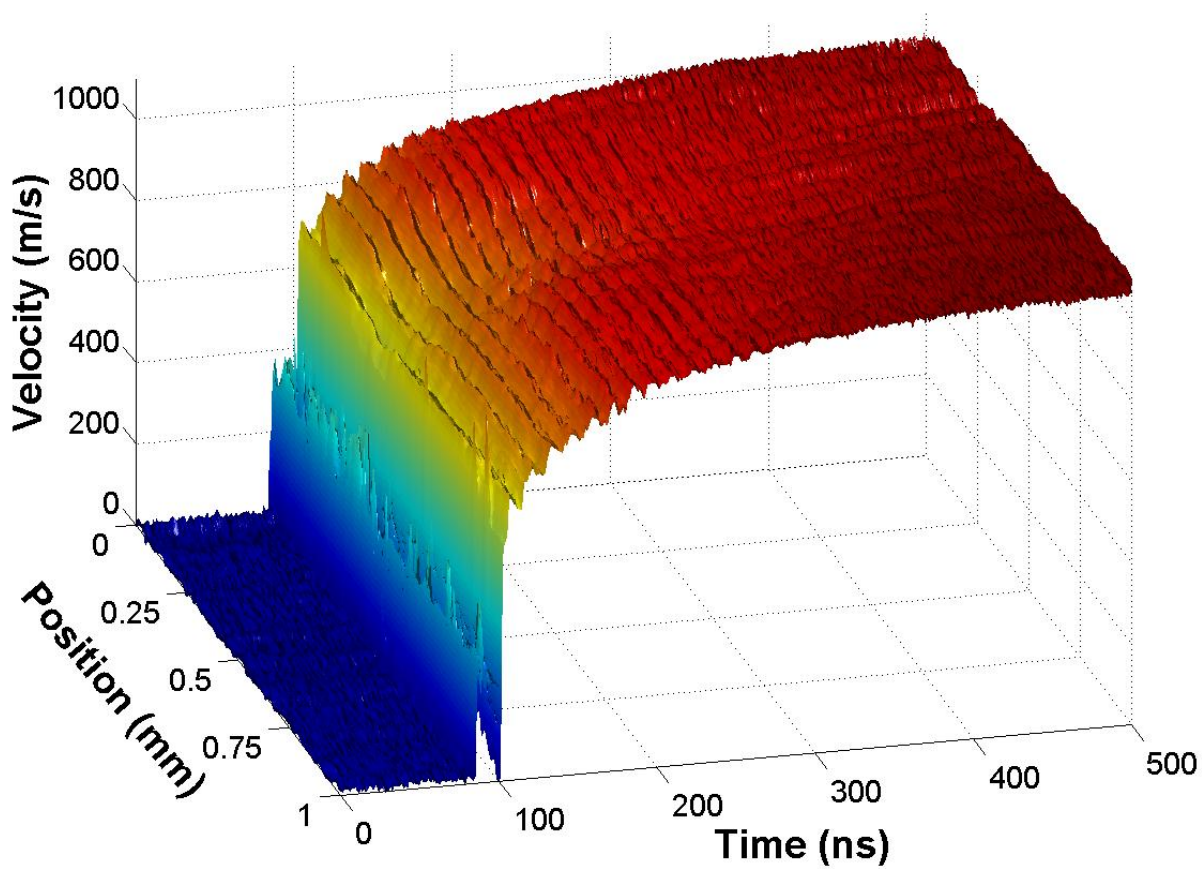
Figure 4.4 Velocity surface, laser-driven flyer

4.3   Conventional Projectile Experiments

These experiments were essentially repeats of previous single-point-VISAR recordings, in order to elucidate the accuracy of the line-VISAR. In both of the recordings, the line-VISAR shows lower temporal resolution and susceptibility to systematic errors in velocity. As the raw streak images show (Figs. 4.5, 4.6), the shock-induced ramp makes up only about 5% of the time window. Although faster streak rates were available, they were not used for fear of missing the event.
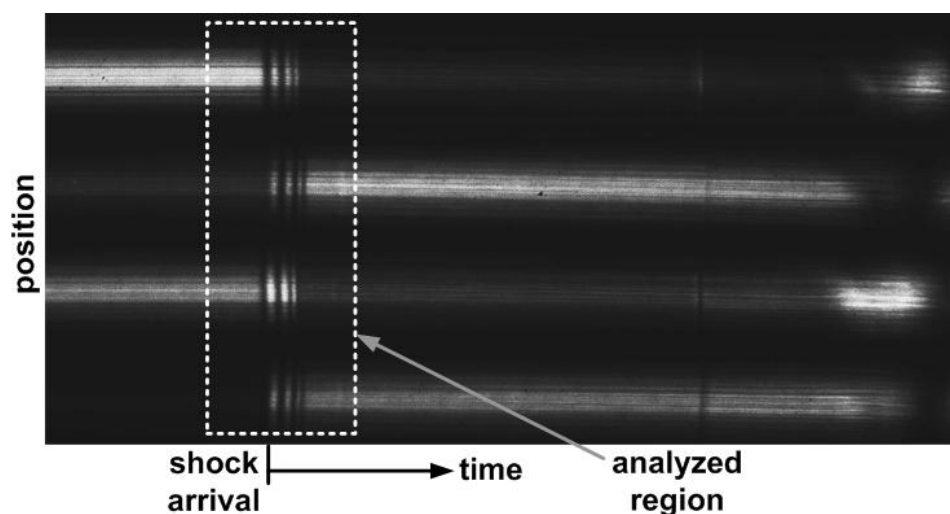
Figure 4.5 Raw streak image, fused silica target

Fig. 4.9 and Fig. 4.10 show velocity averages of a $200\,\mu$m strip about the position center-line of the line-VISAR records. This produces a velocity vs. time plot which is superimposed on the previous single point records. In this comparison, the poor time resolution of the line-VISAR records is especially noticeable for the aluminum target.

There is a growing interest in heterogeneous materials in the shock community, and line-VISAR systems are already being used in their characterization[6, 7, 8]. The main characterization has been velocity variation with position. This is obtainable from single-point-VISAR recordings by examination of the fringe contrast, but the contrast depends only on velocity variation to second order and it is difficult to isolate contrast from detector response. On the other hand, line-VISAR offers a direct measurement of velocity variations in position. Aluminum
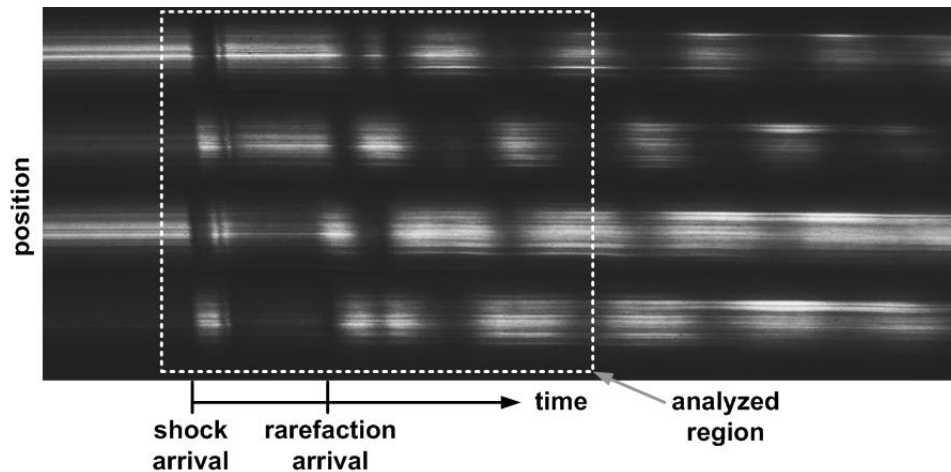
Figure 4.6 Raw streak image, aluminum target

targets are expected to show velocity variation originating from the grain boundaries within the metal. The aluminum impactor was designed to induce spall (seperation) within the aluminum target, which should significantly increase the velocity variation[17]. This information reaches the reflecting surface at a time of approximately $0.4\,\mu$s. In Fig. 4.11, the standard deviation of velocity over a $200\,\mu$m wide strip is plotted. This is the same strip that was used to compute the average velocity. The velocity variation seems consistent with expectations, despite a high level of background noise.

4.4 Consideration of Path Attenuations

Before the experiments with gas-driven projectiles were performed, it was observed that the components of the re-combined images at the camera were not equal in intensity. This led to consideration of the attenuations of the eight distinct paths through the interferometer and the four-to-one relay. The new analysis technique, detailed in subsection 2.4.3, requires two preshot images to obtain the path attenuations. One image is taken with one of the interferometer legs blocked and then a second image is taken with the opposite interferometer leg blocked. All preshot images were taken within a few minutes of the actual experiment in order minimize alignment drift.
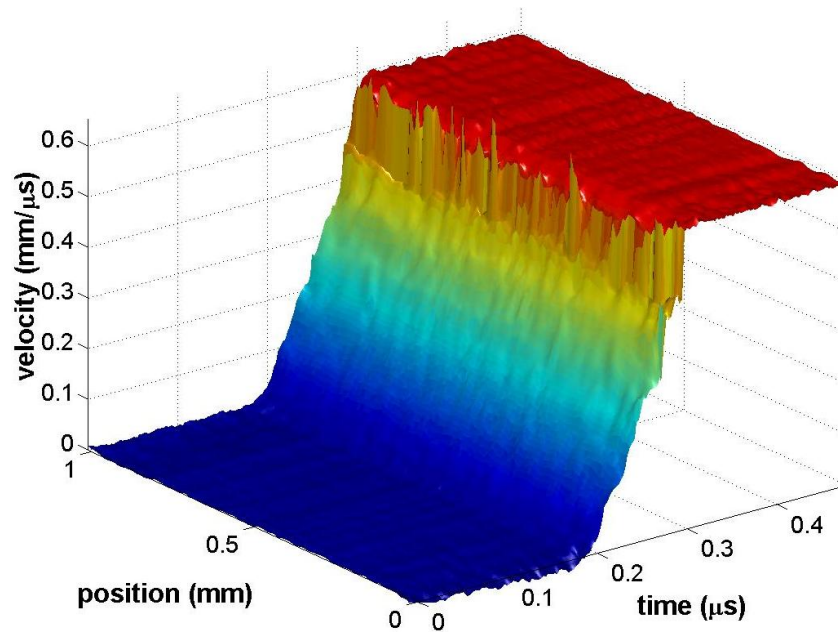
Figure 4.7 Velocity surface, fused silica target
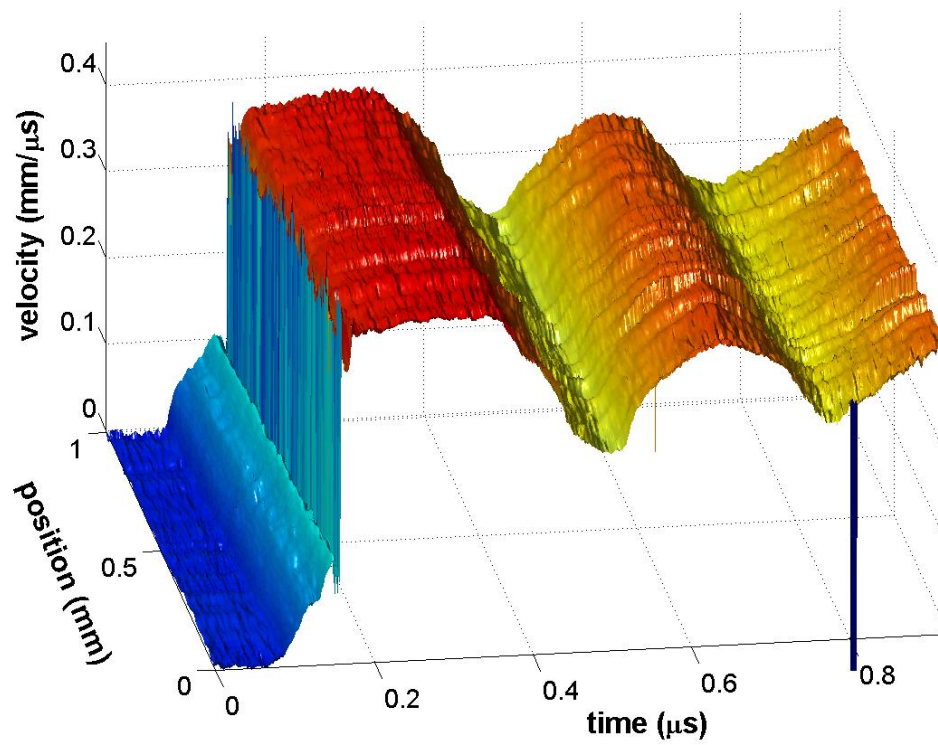
Figure 4.8 Velocity surface, aluminum target
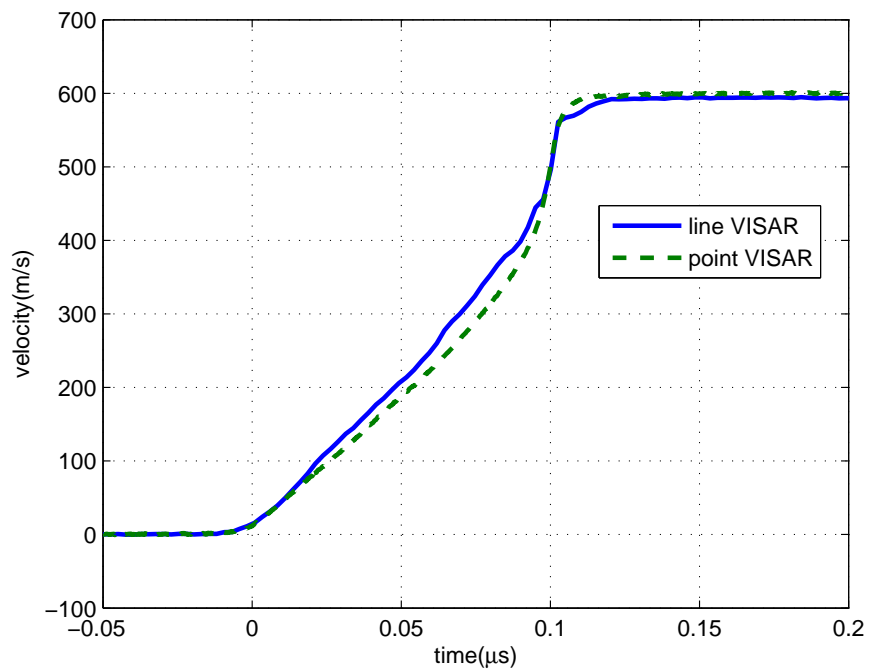
Figure 4.9 Line-VISAR vs. point-VISAR: fused silica target
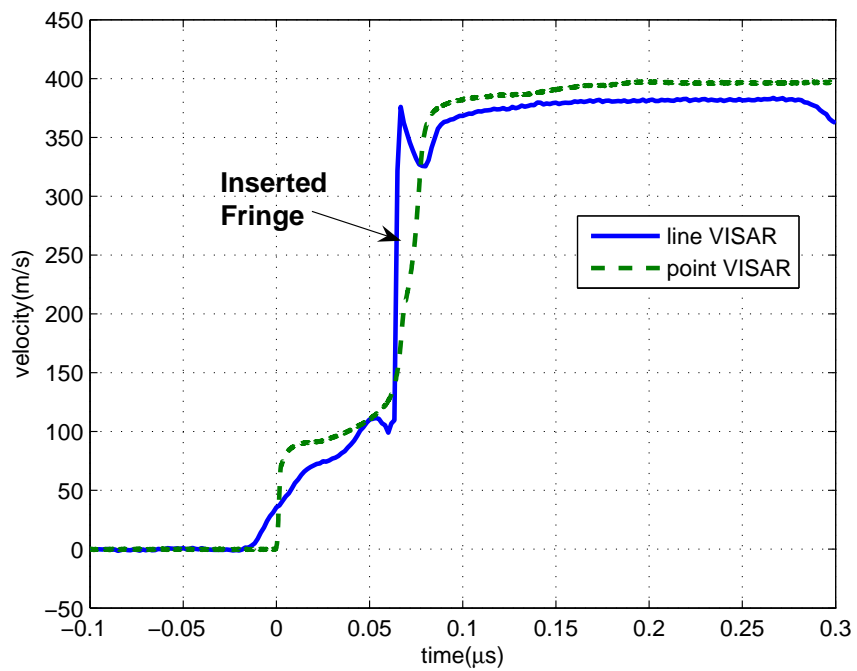
Figure 4.10 Line-VISAR vs. point-VISAR: aluminum target
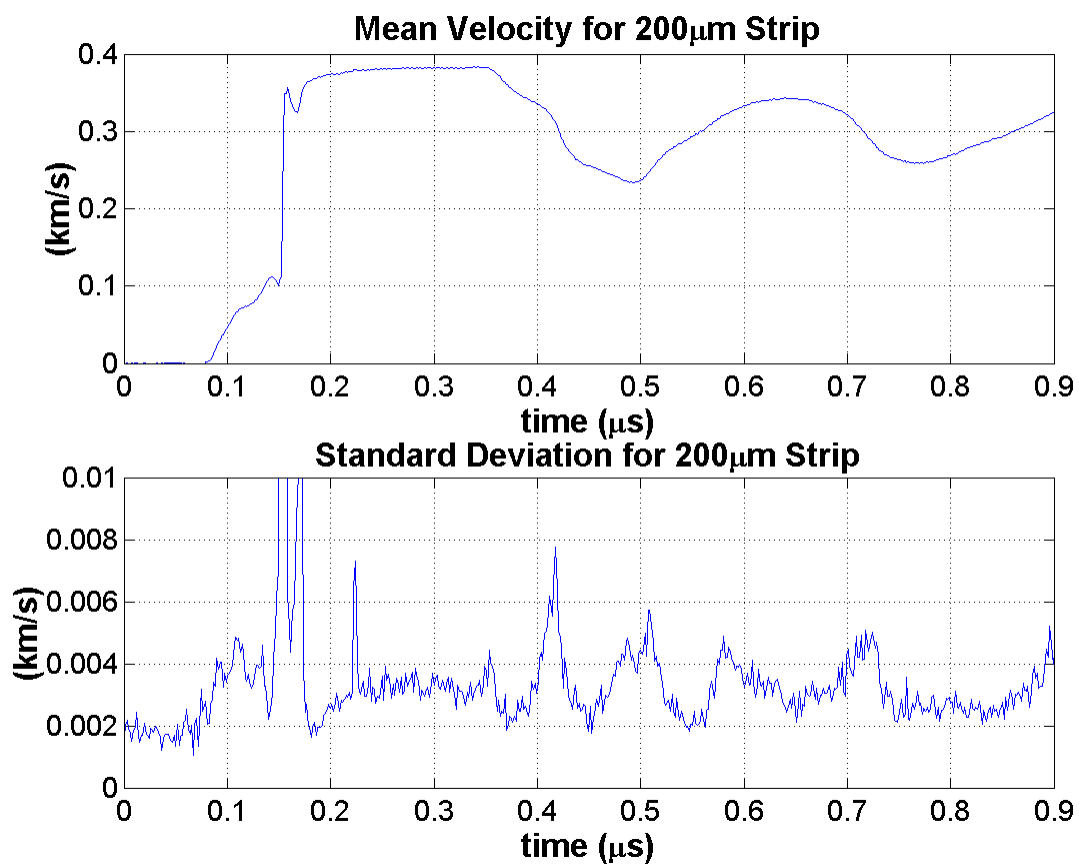
Figure 4.11 Velocity variation, aluminum target

In practice, the image intensities did not always fit well into this type of analysis. A poor fit is evident when the summed intensity signal from a $180°$ pair of quadrature images, weighted by path attenuations, correlates with one of the individual quadrature images, instead of remaining constant in time. Note that these plots are shown in the time-alignment step of the analysis software (Appendix A). This may result from incorrect estimates of the path attenuations or the path attenuations may change after impact.

Chapter 5

Summary and Discussion

5.1   Summary

Fig. 5.1 shows a velocity record from a fringe-displacement line-VISAR for comparison purposes[9]. This record depicts the interaction of a shock-wave with a porous sugar sample. The streak image was analyzed using the software package *VISAR2k*, written by J. J. O'Hare and W. M. Trott at Sandia National Laboratories (SNL)[18]. For comparison purposes, refer to the analyzed velocity records from the quadrature push-pull line-VISAR at WSU, shown in figs. 4.4, 4.7 and 4.8. These records were analyzed by the software package *linevisar*, written at WSU by Dirk Robinson and discussed in Appendix A.

Interferometry is a relative measurement, and an important difference in the analysis techniques is in how the initial phase is determined. The WSU software subtracts an average of the pre-impact phase from the entire record. Thus, the amount of ripple present in the velocity record before the impact event is unchanged and gives an estimate of the precision of this method. In contrast, the analysis method used at SNL subtracts a different phase for each position value in such a way that the velocity surface crosses zero velocity at the time of zero. As shown in Fig. 5.1, the velocity ripple starts at zero time and can be seen growing steadily until impact.

The velocity surface in Fig. 5.1 is used as evidence of variations in velocity induced by a heterogeneous material. However, the velocity surface shows a ripple that grows with time. This ripple is relatively large even before impact, which occurs at approximately $1.5\,\mu$s. The
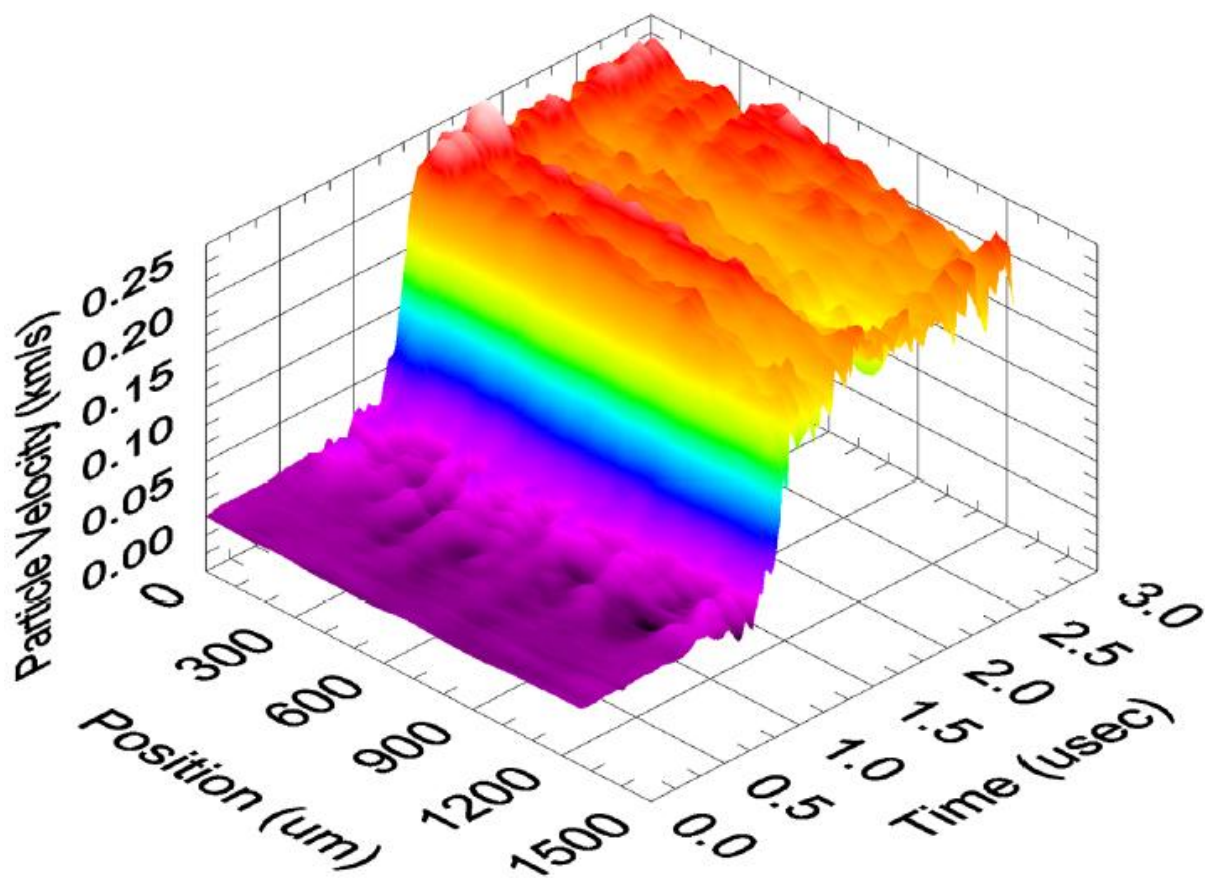
Figure 5.1 Fringe-displacement line-VISAR analyzed velocity record[8]

method for determining the initial phase accounts for some of this growth, so it is unclear what portion of the ripple should be interpreted as velocity variation.

Consider the velocity surface from the symmetric-impact fused silica target Fig. 4.7. As fused silica is a homogeneous material, the velocity variation with position was expected to be minimal throughout the recording. This is observed in the experimental record, since the apparent ripple in velocity from the post-impact region is comparable to the pre-impact region. The pre-impact ripple in velocity is lower in magnitude than in the SNL record by an order of magnitude.

The only system with comparable velocity resolution to the WSU system is the fiber-relayed quadrature design by W. F. Hemsing, discussed in section 2.2.2. However, the averaging and distorting effects of the fiber relays should make the WSU system marginally superior. Still, systematic errors prevent the absolute velocity accuracy of line-VISAR from reaching the level of single-point VISAR.

The use of a streak camera for recording reduces the signal-to-noise ratio and generates several systematic errors. Light sensitivity and background level vary smoothly with position on the input and output phosphor screens. Also, the motion of the streak is generally not a perfectly straight line. These three errors are well compensated for by the analysis software. However, the streak camera response is also locally-varying, non-linear and history dependent. These more difficult issues lead to incorrect estimates of the light path attenuations. The result is a velocity profile which differs in shape from the true history of the surface.

5.2 Improving Data Quality

5.2.1 Increasing Laser Power

The power of the illuminating laser limits the signal-to-noise ratio for lines of about 1 mm and longer. As shown in Table 3.2, the numerical (angular) aperture decreases with increased line length, so there is a significant drop in light-collection efficiency for line lengths above 1 mm. A stronger source laser would increase the signal level at the lower magnifications.

5.2.2 Wide Format Streak Camera

Although the system was designed for use with a 25 mm wide input streak camera, all of the recordings for this thesis were taken with a 9 mm streak camera. Nevertheless, the spatial resolution is already comparable to fringe-displacement line-VISAR recordings using 25 mm streak cameras.

The spatial resolution increases linearly with the width of the streak camera input. The only difficulty is that the setup camera has an active width of only 7.7 mm, which would make it more difficult to align the quadrature images. Attaching a 3:1 or 4:1 image reducer to the setup camera would be useful if a 25 mm streak camera is used.

5.3 Future Work

5.3.1 Timing Fiducial

The nominal streak rate settings are accurate only to about 10%. Also, the streak rate varies somewhat at different points along the time dimension. Thus, a timing fiducial would be necessary to accurately measure the time of events in the streak record. A timing fiducial is a series of pulses of light separated by a fixed time interval. The fiducial is generally recorded beside the interference images, so the useful recording area is slightly reduced. A suggested insertion point for the timing fiducial is from the left side of the main beamsplitter, as shown in Fig. 3.1. A laser diode with a short coherence time would be preferable for this purpose, since it would not exhibit interference.

The fiducial would be split into four images in the same manner as the quadrature images. Thus, the fiducial could also be used to align the quadrature images in position and time. Currently, the speckle pattern caused by reflection from a diffuse target provides a reliable alignment of the quadrature images in position, but the alignment of the images in time can be challenging.

With a timing fiducial it would be possible to measure times to within one image pixel. Since the record length is 1,300 pixels, time intervals could be measured to an accuracy of approximately 1%, for intervals which take up 10% of the total time window.

5.3.2   Framing Camera Experiments

A framing camera is device made to capture a sequence of images in very rapid succession. Unlike a streak camera, which resolves one spatial dimension and has continuous time resolution, a framing camera resolves two spatial dimensions at discrete time instances. Newer framing cameras also have the advantage that they do not rely on electron-optics. Thus, they are inherently free of the image distortions and limited spatial resolution characteristic of streak cameras.

The name area-VISAR is suggested for the technique of VISAR recording using a framing camera. Many of the topics calling for line-VISAR recordings would benefit from the data-rich recordings that are possible with area-VISAR. For example, it would be possible to obtain a velocity record for the entire surface of the laser flyer at about 16 time points. In comparison, line-VISAR allows continuous temporal resolution, but only for a single line along the surface of the flyer.

The optical relay system used in the WSU design makes for a unique feature among line-VISARs: it is very easy to convert the instrument into an area-VISAR. The quadrature images can be arranged in a rectangular array to maximize the use of the framing camera's active area. The two-level construction of the WSU system would also help the conversion to area-VISAR. There is ample room on the top level for a framing camera, despite the fact that framing cameras are typically much larger than streak cameras.

List of References

[1] E. Hecht. *Optics, Fourth Edition*. Addison Wesley, 2002.

[2] D. R. Goosman. Analysis of the laser velocity interferometer. *Journal of Applied Physics*, 46(8):3416–24, August 1975.

[3] L. M. Barker and R. E. Hollenbach. Laser interferometer for measuring high velocities of any reflecting surface. *Journal of Applied Physics*, 43(11):4669–75, November 1972.

[4] W. F. Hemsing et al. VISAR: Line-imaging interferometer. In *SPIE 1346* [19], pages 133–40.

[5] D. D. Bloomquist and S. A. Sheffield. Optically recording interferometer for velocity measurements with subnanosecond resolution. *Journal of Applied Physics*, 54(4):1717–22, 1983.

[6] W. M. Trott et al. Measurements of spatially resolved velocity variations in shock compressed heterogeneous materials using a line-imaging velocity interferometer. In *SCCM 1999*, pages 993–98. American Physical Society Conference Proceedings, 1999.

[7] M. R. Baer and W. M. Trott. Mesoscale descriptions of shock-loaded heterogeneous materials. In *SCCM 2001* [20], pages 713–16.

[8] W. M. Trott et al. Investigation of dispersive waves in low-density sugar and HMX using line-imaging velocity interferometry. In *SCCM 2001* [20], pages 845–48.

[9] P. Celiers, W. Trott, and W. Hemsing. NIF: VISAR interferometer meeting (handout, unpublished). Technical Report LLNL-B391, R1200, Lawrence Livermore National Laboratories, 2002.

[10] B. E. A. Saleh and M. C. Teich. *Fundamentals of Photonics*. Wiley-Interscience, 1991.

[11] W. F. Hemsing. VISAR: Displacement-mode data reduction. In *SPIE 1346* [19], pages 141–50.

[12] L. M. Barker and K. W. Schuler. Correction to the velocity-per-fringe relationship for the VISAR interferometer. *Journal of Applied Physics*, 45(8):3692–93, August 1974.

[13] R. E. Fischer and B. Tadic-Galeb. *Optical System Design*. McGraw-Hill, 2000.

[14] ZEMAX optical design program, version 10.0, 2001. Focus Software, Inc. www.focus-software.com.

[15] L. M. Barker and R. E. Hollenbach. Shock-wave studies of PMMA, fused silica, and sapphire. *Journal of Applied Physics*, 41(10):4208–26, September 1970.

[16] K. Zimmerman. Private communication.

[17] L. C. Chhabildas et al. Incipent spall studies in tantalum – microstructural effects. In *SCCM 2001* [20], pages 483–86.

[18] J. J. O'Hare and W. M. Trott. VISAR2K version 1.0 beta – user's manual. Technical report, Sandia National Laboratories, January 2003.

[19] SPIE. *Ultrahigh- and high-speed photography, videography, photonics, and velocimetry '90*, volume 1346, 1990.

[20] American Physical Society Conference Proceedings. *Shock Compression of Condensed Matter*, 2001.

[21] D. C. Ghiglia and M. D. Pritt. *Two-Dimensional Phase Unwrapping: Theory, Algorithms, and Software*. Wiley, 1998.

[22] L. M. Barker. *in Behavior of Dense Media Under High Dynamic Pressures*, page 483. Gordon and Breach, New York, 1968.

[23] G. F. Raiser. Background and data reduction on the SDC VISAR. Internal report, Institute for Shock Physics, Washington State University, October 1994.

[24] MATLAB, version 6.3, 2003. The MathWorks, Inc. www.mathworks.com.

[25] W. H. Press. *Numerical Recipes in C: the Art of Scientific Computing*. Cambridge University Press, 1992.

Appendix A:
User's Guide to the Line-VISAR Analysis Software

A.1   Introduction

An analysis program, `linevisar`, was written in MATLAB to reduce data from push-pull line-VISAR instruments. This program accounts for non-uniform attenuation of the eight paths from the target through the VISAR system to the camera. This requires recording two preshot streak images with the left and then the right leg of the interferometer blocked before the shot itself. Then, the user must align the four quadrature images in position and time. The remainder of the program is similar to single-point VISAR analysis, except that a two-dimensional phase unwrapping technique is used. The unwrapping technique has the ability to identify the location and shape of lost fringe(s), or a velocity jump.

A.2   Overview

The analysis program is constructed as a series of graphical user interfaces (GUIs). At each step, the user may proceed to the next GUI or return to the previous GUI. The analysis program involves the eight fundamental steps:

1. Load preshot and shot streak images, apply filters, subtract estimated background

2. Align the quadrature images in time

3. Align the quadrature images in position

4. Show Lisajou line-outs, allow user to enter ϕ, select region of interest

5. Calculate phase, contrast, signal strength

6. Unwrap the phase, insert jumps

7. Determine τ, *vpf* from experiment parameters

8. Calculate velocity and display, save results to the base MATLAB workspace

Most of the analysis steps involve interaction with the user, which will be further explained below.

A.3　Major Analysis Steps

A.3.1　Step 1: Load images, filter, subtract background

Fig. A.1 shows the first step in the analysis, in which the user chooses the two non-interfered preshot images and the shot image. In the following discussion, the term *column* denotes a set of pixels in the image with a fixed time value (vertical line), while *row* denotes a set of pixels with a common position (horizontal line).

When one of the preshot images is loaded, it is separated into four images by dividing it with boundary curves. All five boundaries are fit to the same second-order polynomial of position with respect to time. This estimates the time-dependent position drift of the streak camera. The bounding curved lines are shown in light-green in Fig. A.1.

After the image boundaries are obtained, they are used to correct the position drift of the streak camera. Each column in the image is shifted in position according to the boundary polynomial, to produce a "straightened" image. Next, the image is summed over time for each position, producing a summed intensity curve similar to that shown in Fig. A.2. A second order polynomial is then fit through the boundary points, which is the estimated background of Fig. A.2. Between each pair of consecutive boundary points, the sum of the counts between the two curves is used as the path responsivity, or attenuation. There are a total of eight path responsivities which are stored for later use in the analysis.

When the shot image is loaded, the shot image boundaries are set to the average of the two preshot boundaries. If preshot images are not provided, analysis can still proceed but the
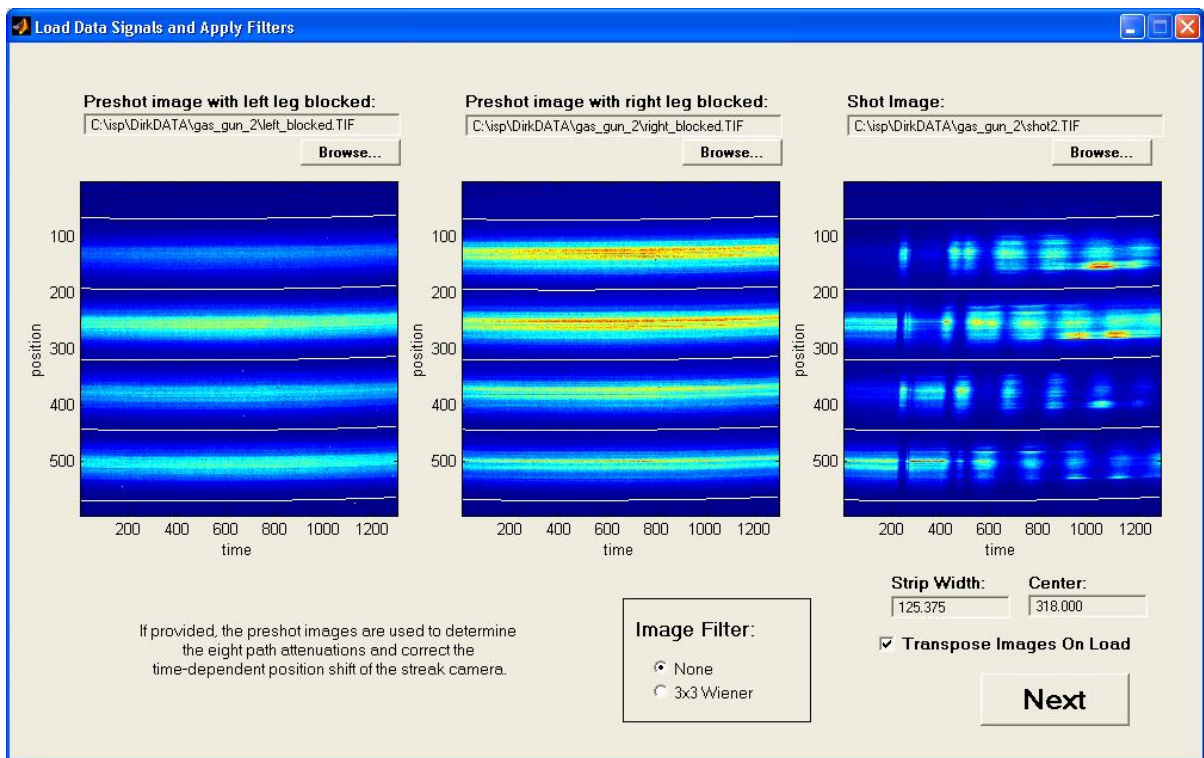
Figure A.1 Load images GUI. Left, center – preshot (non-interfered) images used to find boundaries and responsivities. Right – shot image
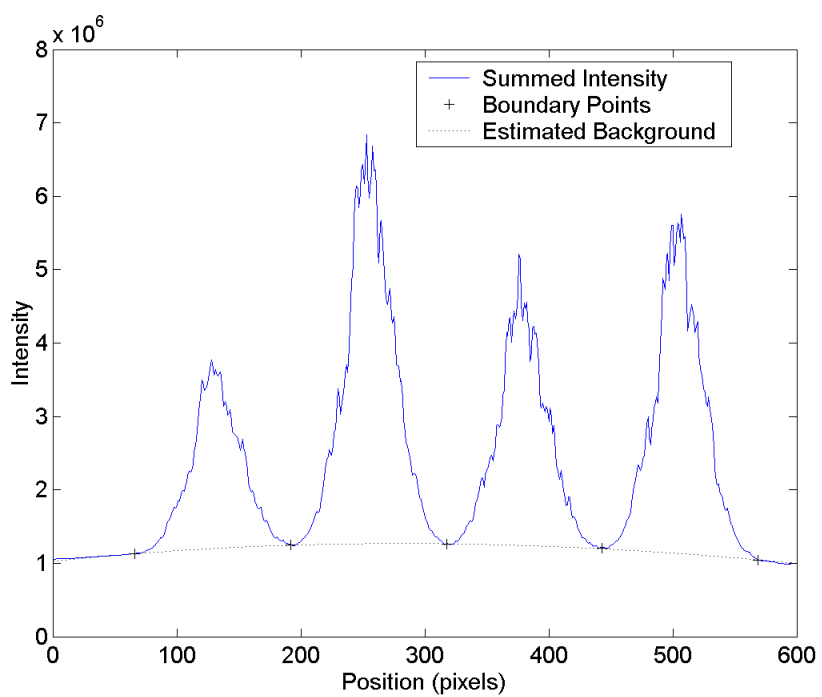
Figure A.2 Estimation of the background for a preshot image. Intensity is summed over time.

streak camera drift and path attenuations will not be corrected for. When preshot images are not loaded, the image boundaries are straight lines of constant position.

Text boxes are provided to manually set the boundaries of the image if the estimated boundaries are not adequate. This has not been necessary experiments up to the point of this writing.

When the user pushes the "Next" button, the selected image filter is applied to the image. The image is then corrected for time-dependent position drift. Then, the intensity level along each of the five image boundaries is copied to memory, where it is smoothed by an 101-point continuous average filter. The resulting smoothed intensity signals are shown in Fig. A.3. Next, for each column of the image, a second order polynomial in position is fit to the smoothed image boundary curve values at the corresponding time. This polynomial represents the estimated background at that time, which is subtracted from the image column. An example background estimate for the 600th column is shown in Fig. A.4.
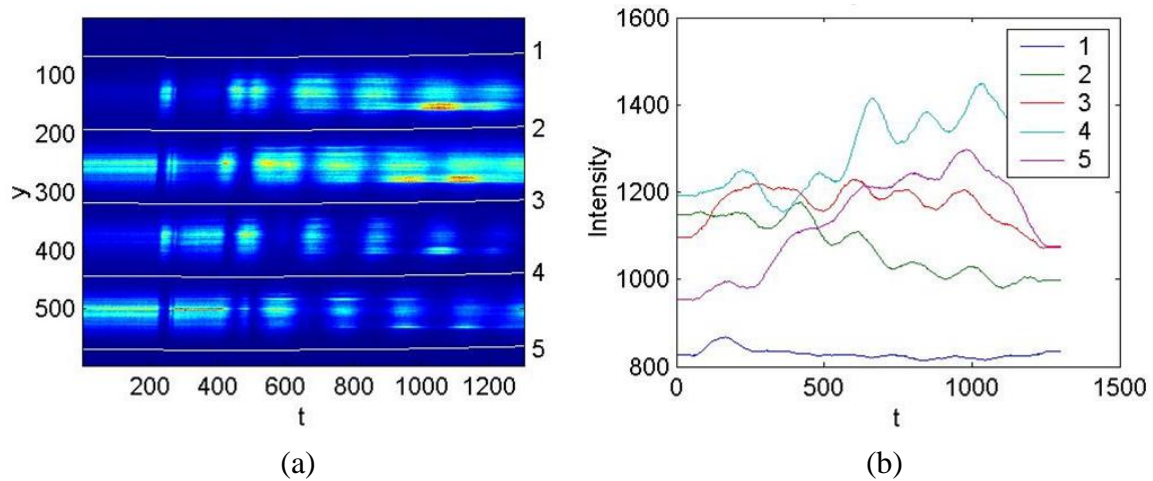
Figure A.3 (a) Shot image divided into four quadrature images according to boundaries obtained with preshot images. (b) Intensity along the five boundary lines, after 101-point continuous average filter.

A.3.2   Step 2: Alignment of quadrature images in time

The second major step in the analysis is to align the quadrature images in time and correct their tilts on the streak camera. This is performed in three minor steps.
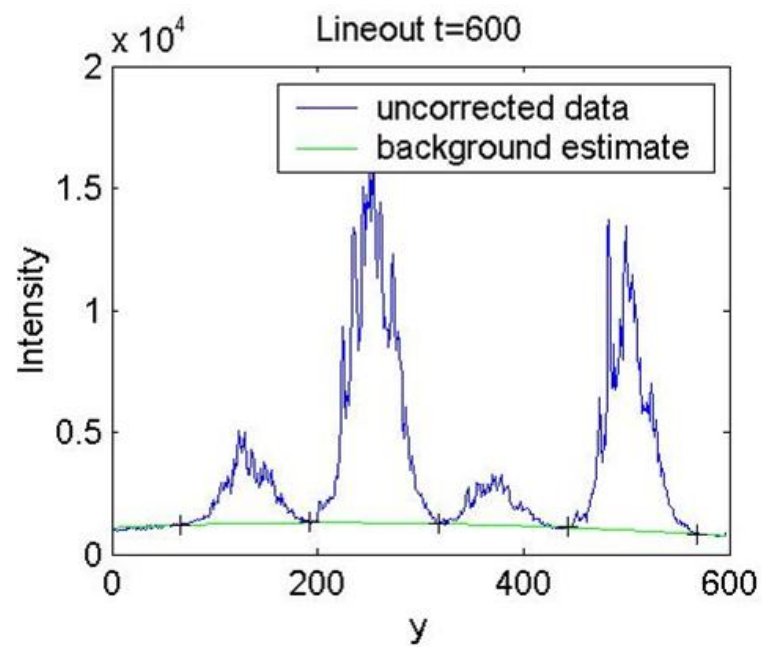
Figure A.4 Estimated background for the shot image for the column t=600 pixels. The cross-hairs locations are from the smoothed boundary intensities shown in Fig. A.3(b).

Align sin **pair of images in time**

First, the sin pair of images, which are the two outside images, are aligned with respect to one another in time. This pair of images has a phase separation of exactly $180°$. Thus, the sum of the two images should be nearly constant in time, when weighted for path responsivities. The sin and $-\sin$ quadrature images are shown at the left in Fig. A.5(a). However, it is generally easiest to work with the intensity signals that are summed over position on the large plot window. The time interval of the images at the left is shown by a dashed-line rectangle in this plot. The interval can be adjusted by dragging the sides of the rectangle with the mouse. The automatic alignment in time works best when the fit interval contains the most dynamic part of the signals, as shown by the dashed rectangles in Fig. A.5.

This GUI and several others in the analysis package offers a zoom mode to zoom along one or both axes of a plot. When zoom is on, click anywhere on the record and drag to set the new axes limits. Double clicking will restore the axes limits to the extents of the data. Typing `help zoom` at the MATLAB command window will give a full description of the zoom interface.

After this window loads, it is recommended to set the time interval and push the "Fit Offset" button. This uses optimization to set t_{41}, that is, the relative time offset of the $-\sin$ image with respect to the sin image. The optimization criterion is set by comparing the weighted sin sum, $I_{\sin} + I_{-\sin}$, to a fourth-order polynomial smoothed estimate of itself. The integrated-squared-distance between this signal and its estimate is locally minimized. This effectively minimizes the variation of the summed signal with time.

When the initial time offset is more than a few pixels, the optimizer often goes to the wrong local minimum. In this case, the features of $I_{\sin}$ and $I_{-\sin}$ will appear significantly misaligned. If this occurs, manually set the offset and run the fit again.

After the sin pair of images are aligned in time, the user can optionally fit the respective image tilts. Instead of using the entire image summed over position as with fitting the offset, this step takes one sum from the top rows of the image and one from the bottom. The respective tilts of the sin and $-\sin$ images are varied symmetrically to optimize the weighted sin sum signals from both the top and bottom of the image simultaneously.
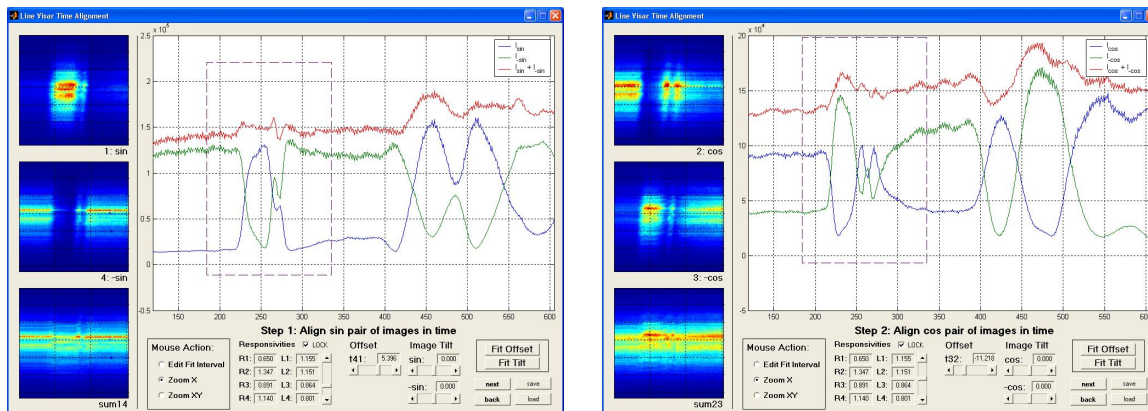
(a)   (b)
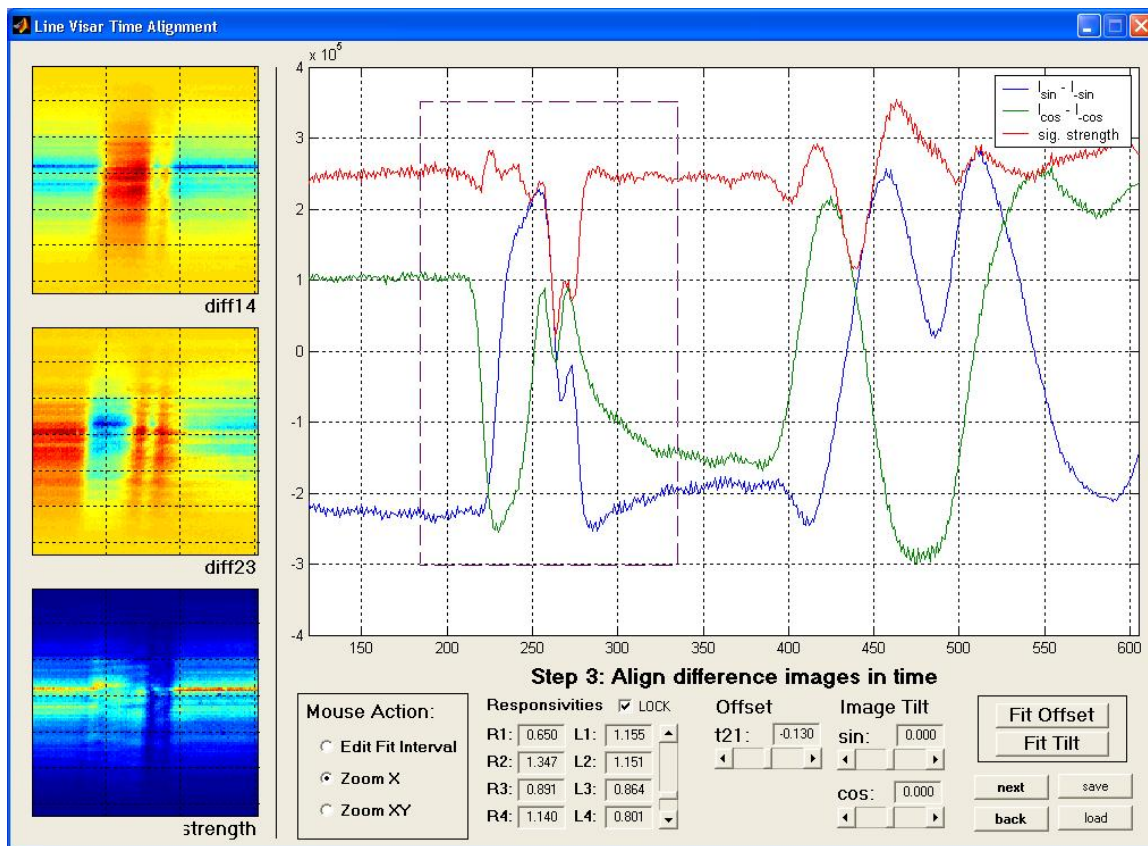
(c)

Figure A.5 Time alignment GUI: (a) sin pair of images, (b) cos pair, (c) sin pair difference with cos pair difference

As an advanced feature, it is possible to manually set the path responsivities. A vertical slider bar is provided which controls the scale of one of the component signals. When in the $\sin$ alignment step, this scales the attenuations R_1 and L_1 by the same factor. This scales the $\sin$ signal while leaving the $-\sin$ unchanged. The user can use the slider bar to minimize the correlation between the summed signal and the two component signals.

Align $\cos$ **pair of images in time**

The alignment of the $\cos$ pair of image in time follows an identical process to that described above. Ideally, the summed signal, $I_{\cos} + I_{-\cos}$ should be identical to the summed signal in the previous minor step, $I_{\sin} + I_{-\sin}$. In this step, the responsivity slider scales R_2 and L_2, which scales the $\cos$ signal, while leaving the $-\cos$ signal fixed.

Align $\sin$ **pair with** $\cos$ **pair**

The final time alignment step is to align the $\sin$ pair of images with respect to the $\cos$ pair. Although the same window layout is used, the alignment procedure is different.

During this step, the attenuation-weighted difference of the $\sin$ images is shown in the upper-left axes of Fig. A.5(c), and the weighted $\cos$ difference is shown at center-left. A new quantity, the signal strength, is shown at lower-left. The signal strength is the result of adding the $\sin$ and $\cos$ images in quadrature. It should remain constant in time except when the signal is limited by the time-response of the streak camera.

As before, the combined images at the left are summed over position to produce the intensity vs. time signals in the large axes. In this step, the optimizer attempts to maximize the smoothness of the two component signals added in quadrature, in the same way that it operated on the linearly added component signals in the above two steps. However, there is generally a high density of local minima, so this step requires more user guidance. The final "signal strength" signal should be nearly constant and not correlate with the features of the other two signals. Note that fast transients will cause the signal strength to dip because of limited time response.

A.3.3 Step 3: Alignment of quadrature images in position

The speckle pattern produced by dispersively reflecting targets makes it relatively easy to align the quadrature images in position. To display the alignment, a three-step process is used. However, the optimization procedure finds all three relative offsets simultaneously.

The optimizer is programmed to maximize the "sharpness" of the linear addition of all four quadrature images. The sharpness is a scalar quantity found by a root-mean-square sum over both time and position.

The optimizer generally does a good job of finding the correct position offsets, although it may require tens of seconds. To help the user verify that the offsets are correct, several signals are plotted in front of images.

In the first position alignment step, Fig. A.6(a), the background image is an attenuation-weighted sum of the $\sin$ and $-\sin$ images. The time-interval of this plot is set during the previous major step, "alignment in time". Overlayed on this plot is the mean-value in position. The mean-value is scaled by a factor of five to make its features more obvious. At the bottom of the image, the relative intensities of the $\sin$ and $-\sin$ images are shown. When the images are well aligned in position, the mean position signal should not correlate with either intensity signal.

Next, the second position alignment step shows the weighted sum of the $\cos$ and $-\cos$ images. Again, the mean position of this image should not correspond to the component intensities.

The final position alignment step is the alignment of the $\sin$ pair of images with the $\cos$ pair, as shown in Fig. A.6. The background image here is the sum of all four quadrature images. Two mean position signals are shown, one for the $\sin$ pair of images and one for the $\sin$ images. These two signals give an impression of the position offset between the two summed image pairs.
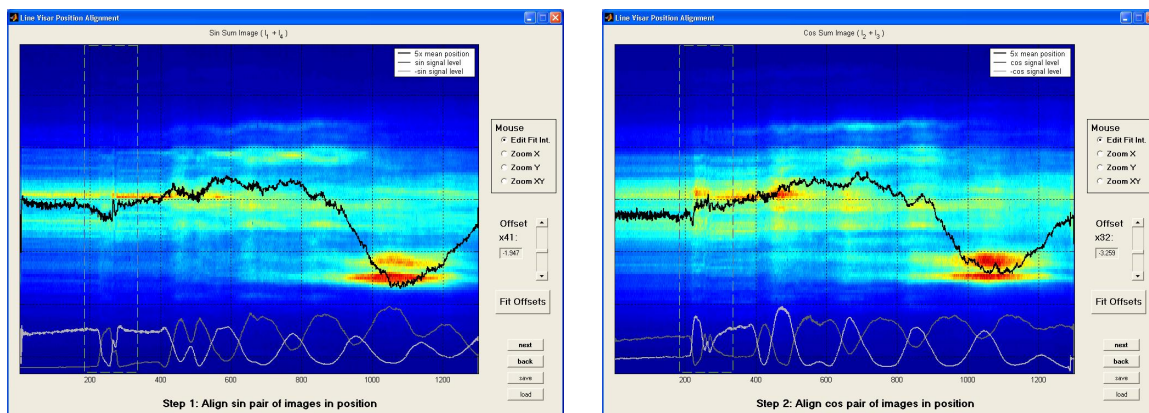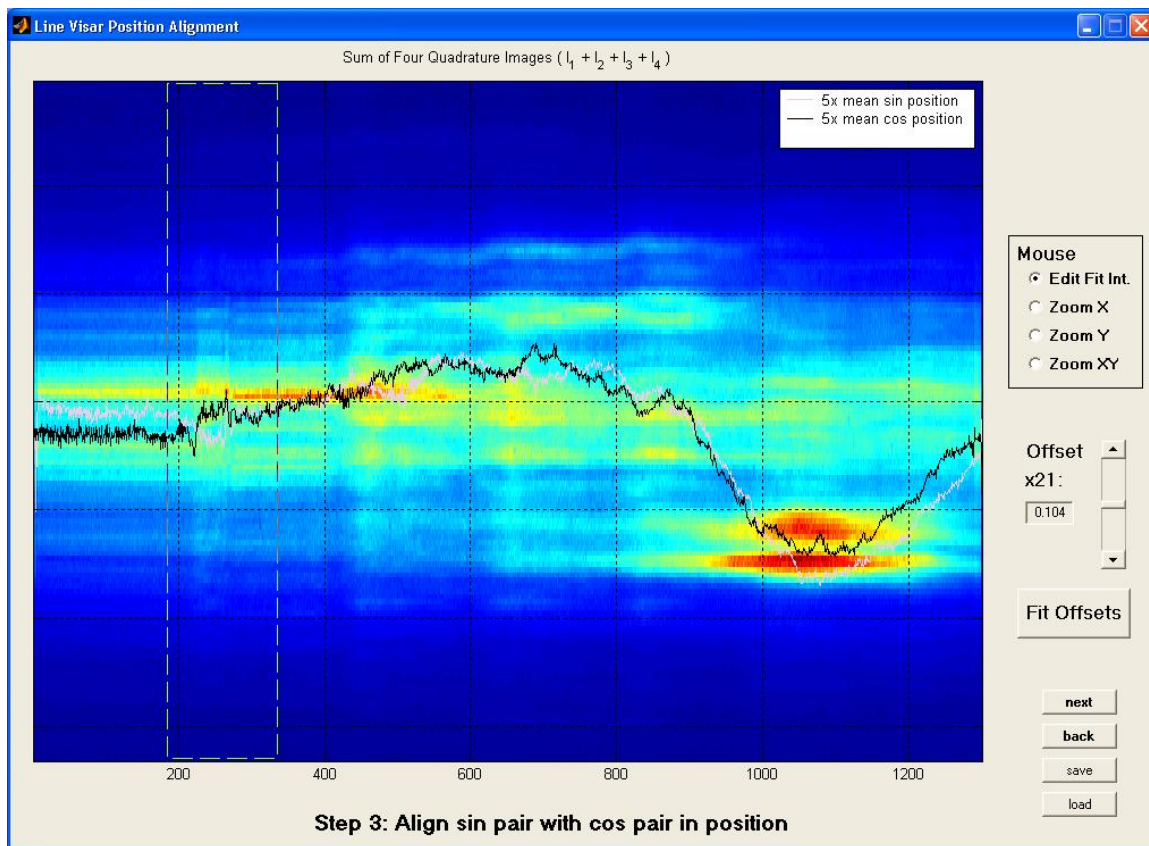
Figure A.6 Position alignment GUI: (a) sin pair of images, (b) cos pair, (c) summed sin pair with summed cos pair

A.3.4   Step 4: Lisajou

The fourth major step of the analysis is the Lisajou display. In this step, the user may adjust ϕ, the phase offset. Another important function of this step is to display the phase history. The phase image is shown at the bottom of the window (Fig. A.7). Overlayed on this image, the positions of the Lisajou "strips" are shown. These strips represent positions lineouts that are averaged over $\frac{1}{11}$ of the image height.

A.3.5   Step 5: Calculation of phase, contrast, and signal strength

The fifth step in the analysis involves the calculation of the phase and contrast. Also, the signal strength is calculated over the region of interest to guide the phase unwrapping process. This calculation follows the sequence detailed in subsection 2.4.3, and is implemented in the top-level file `linevisar.m`.

A.3.6   Step 6: Phase unwrapping

The phase is extracted from the quadrature images using the arctangent, so it initially "wrapped" to the interval $(-\pi, \pi]$. The sixth analysis step unwraps the phase image by adding multiples of 2π to each of the image pixels in a manner which produces a continuous phase surface. The technique of quality-guided phase unwrapping was implemented to perform the unwrapping[21].

With point-VISAR analysis, the unwrapping process proceeds along the time axis, making sure that the phase difference between consecutive pixels in time is π or less. Afterward, the user can insert fringes at time points were the phase difference actually should change by more than π between samples. This process could be applied for each row of constant position in the line-VISAR record, but with hundreds of rows this would be very tedious. At first it might seem that one could simply add the same number of fringes at the same time point to all of the rows. However, the number of fringes to insert tends to vary across the image. Additionally, the unwrapping technique should be able to account for shock fronts which are curved or stepped across position.
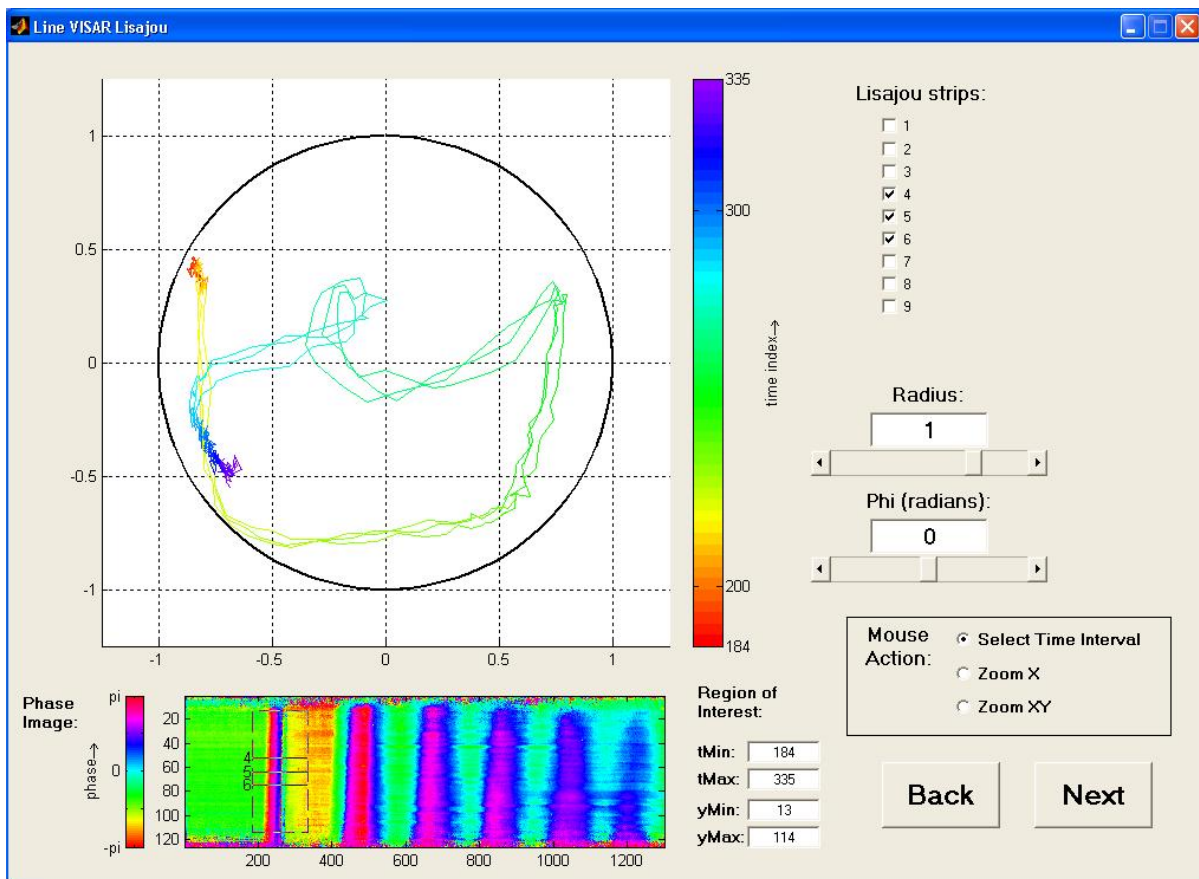
Figure A.7 Lisajou GUI

To simplify the unwrapping process for the user, the unwrapping technique follows the signal strength instead of the time axis. The signal strength is proportional to both the apparent fringe contrast and laser intensity, so it serves as a measure of the signal-to-noise ratio for the phase image. During a fast velocity transient, the apparent fringe contrast drops to near zero due to the time response of the streak camera. This causes the unwrapping process to avoid sharp velocity transients and low-intensity regions until the end, which results in continuous phase surfaces on both sides of the transients.

Quality-guided phase unwrapping begins by marking a single "seed" pixel as unwrapped. Then the pixel surrounding the unwrapped region with the highest quality is unwrapped. This step repeats until all of the image pixels are unwrapped. The unwrapping algorithm simply adds an appropriate multiple of 2π to the pixel being unwrapped so that the phase distance between this pixel and the adjacent unwrapped pixel is π or less. In this application, the signal strength is used as the quality metric.

For application to line-VISAR, the quality-guided technique was expanded to include a second seed pixel. The seeds are labeled as pre-impact and post-impact, and are intended to be placed before and after a sharp velocity transition that may require a fringe insertion. A sharp transition will create a drop in the signal strength due to detector time response. The phase will unwrap into two regions that meet along a curve. This curve is a typically exactly where a fringe insertion should be placed.

Finally, note that a 41×41 pixel square centered about the pre-impact seed pixel is averaged to obtain the initial, or reference phase. The user must ensure that this rectangle contains only pixels that correspond to a stationary target.

Fig. A.8(a) shows the phase unwrapping process as the two regions begin to meet, and (b) shows the completely unwrapped phase. The data shown requires the insertion of one fringe (+1 jump button), which adds a phase of 2π to all image pixels to the right of the black curve.

(a)

(b)
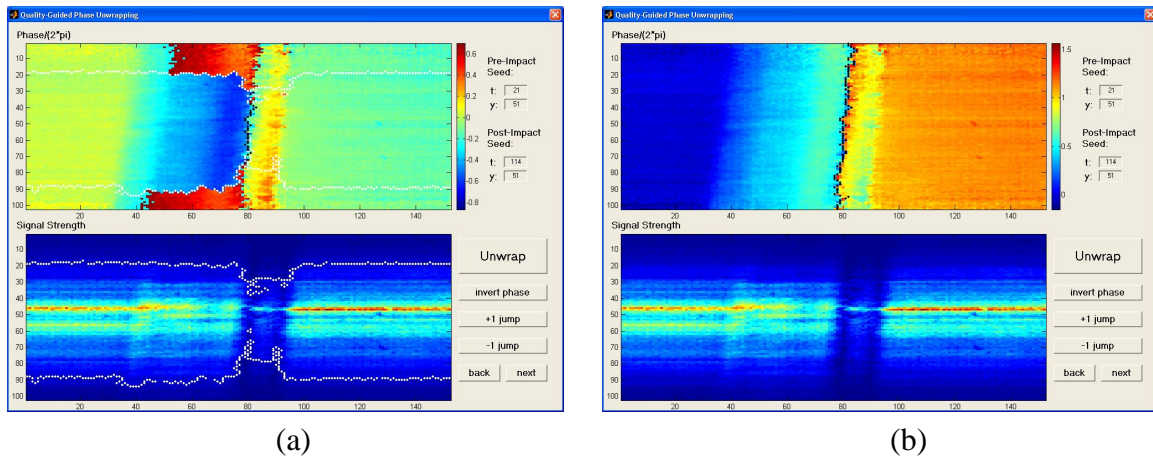
Figure A.8 Phase Unwrapping GUI: (a) unwrapping in progress (b) unwrapping complete, with inserted fringe

A.3.7   Step 7: Experiment Parameters

Analysis step seven asks the user to input the remaining information required to obtain the velocity from the phase image. At the top of the GUI for this step, Fig. A.9, the thicknesses and materials of all delay elements are specified. The refractive index, n, and dispersion index, δ, are specified at each of the available wavelengths in the parameter file optics.txt.
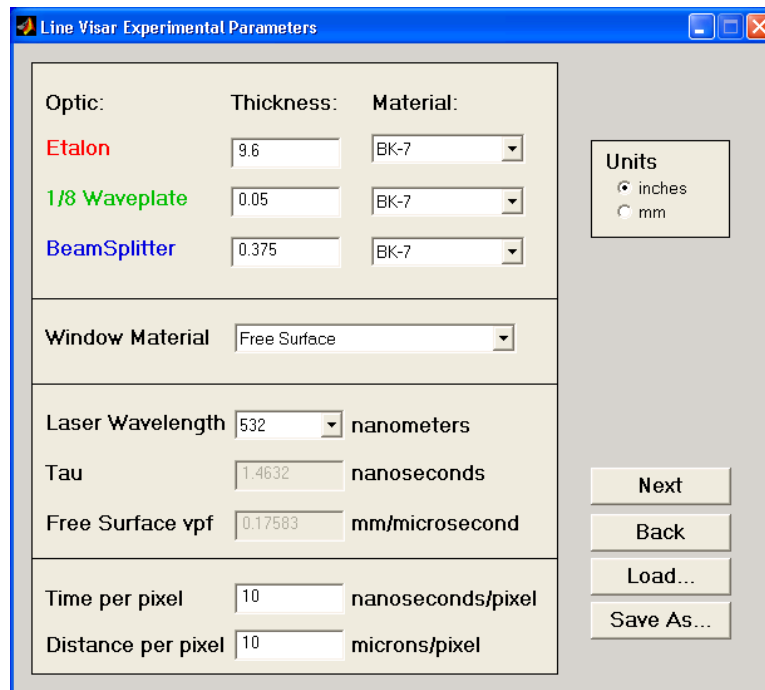
Figure A.9 Experiment Paramesters GUI

The user can also specify a window material if one was used in the experiment. A window material is a transparent material in front of and in contact with the target surface. Recall that the *vpf* is the velocity per fringe constant for a free surface, which means the *vpf* is valid only when no window material is used. The modification to velocity produced by a window material has the form:

$$v(t) = vpf \frac{phase(t)}{2\pi} \frac{1}{1 + \Delta\nu/\nu_0} \tag{A.1}$$

The term $\Delta\nu/\nu_0$ represents the relative change in frequency of the reflected light resulting from shock-wave interaction with the window material[22]. The correction factor is empirically determined, and may be velocity-dependent. New window materials can be added to the software by adding lines to the file `windows.txt`. The window corrections already listed in `windows.txt` were extracted from the current single-point VISAR analysis software at WSU[23].

Lastly, the user specifies the time and distance per pixel. These are used to provide the appropriate axis labels on the final velocity surface plot.

A.3.8   Step 8: Calculation and display of velocity

The final major step in the analysis is to use the experiment parameters to calculate the velocity from the phase. This proceeds according to Eq. A.1, where the *vpf* constant is determined assuming optically equivalence of the interferometer legs, as described in subsection 2.4.2. If the correction factor $\Delta\nu/\nu_0$ is velocity dependent, the velocity calculation proceeds iteratively until the maximum change in velocity at any pixel is less than 10^{-9}.

The velocity surface is then plotted, and the user is given a last chance to go back to the previous analysis steps to change parameters. At the end of this step, the two-dimensional array of velocity data is saved to the base MATLAB workspace, along with data for the time and position axes.

Appendix B:
Software Reference

B.1   Overview

The `linevisar` software consists of MATLAB `.m` program files, `.fig` files describing window layouts, `.mat` binary data files and `.txt` plain-text parameter storing files. The hierarchy of these files is shown in Fig. B.1 and Fig. B.2. The analysis proceeds in eight major steps. Six of the steps use graphical user interfaces, or GUIs. In MATLAB, GUIs are described with a `.fig` file to describe the graphical window and a `.m` file of the same name to program responses to mouse and keyboard input. The top level program is the file `linevisar.m`, which controls execution of the eight steps. This modular design style enables users to easily replace, modify or add steps as needed.

B.2   Brief Introduction to MATLAB GUI Programming

The non-sequential nature of GUI programming may be confusing to newcomers, so here are a few guidelines for creating `.fig`–`.m` GUIs in MATLAB.

- The main function at the beginning of the `.m` file file is essentially a dispatcher so that events such as mouse clicks on buttons can be associated with one of the 'callback' functions listed below it. The other tasks of the main function are to handle the initialization and cleanup of the GUI.

- In the `linevisar` software, a GUI is given the message to display and initialize itself by passing the string 'begin' as its first argument along with other initialization data (see `linevisar.m`).

main

linevisar.m

analysis steps

lv_get_files.m **lv_get_files.fig**	**lv_time_align.m** **lv_time_align.fig**	**lv_position_align.m** **lv_position_align.fig**	**lv_lisajou.m** **lv_lisajou.fig**

helper functions

lv_boxcar.m **lv_fivebound.m** **lv_get_response.m** **lv_image_straighten.m**	**amoeba.m**	**sin_sum.m** **cos_sum.m** **sin_diff.m** **cos_diff.m**	**lv_rect.m**
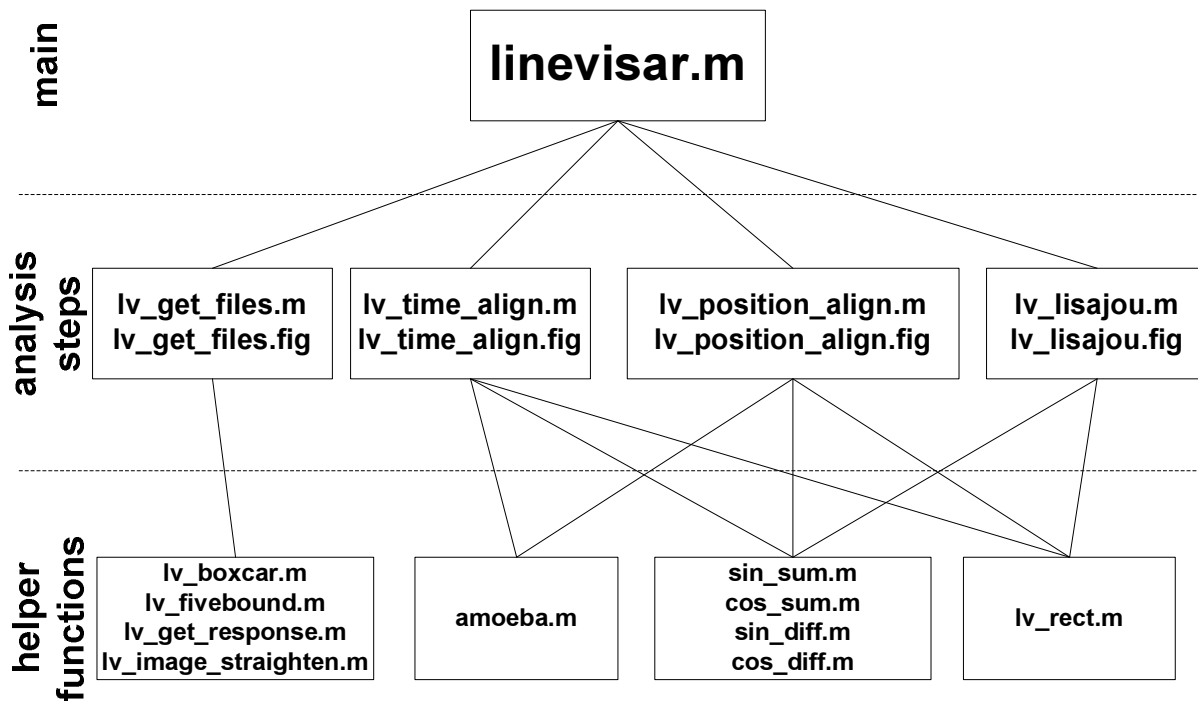
Figure B.1 Software Heirarchy, steps 1–4

main

linevisar.m

analysis steps

qual_unwrap_visual.m **qual_unwrap_visual.fig**	**lv_experiment_params.m** **lv_experiment_params.fig**	**calc_velocity.m**

data and parameter files

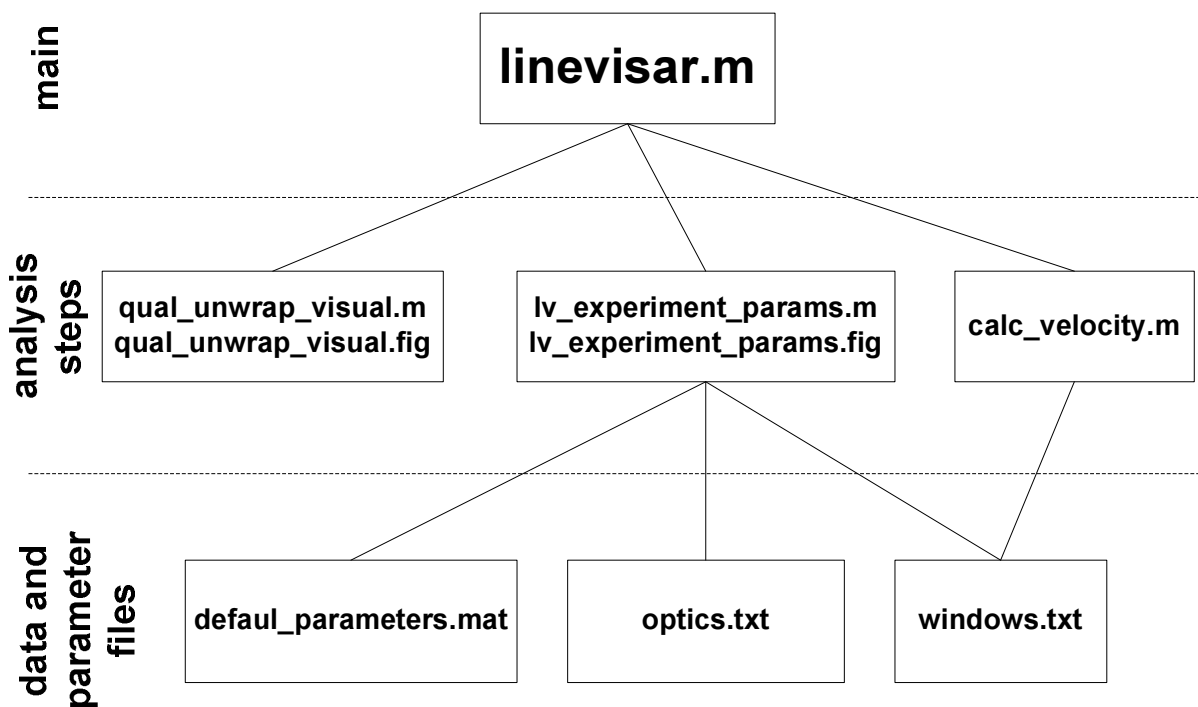|		
defaul_parameters.mat	**optics.txt**	**windows.txt**

Figure B.2 Software Heirarchy, steps 5–8

- To share data between callbacks, the data are copied to variables which are attached to the structure 'handles'. This variable is then copied to the user data of the GUI figure, where the data remains valid until the figure is closed. This structure also contains the handles of the figure and all its "children", or graphical objects that the figure contains.

- Additional information can be obtained in the 'Creating Graphical User Interfaces' manual packaged with MATLAB[24].

B.3   Main - `linevisar.m`

The top level file contains the function `linevisar`, which is called by the user at the MATLAB command line. This function calls the major analysis steps in order, with the ability to go backward to previous steps. Most of the analysis is left to the dedicated functions for each of the steps.

Step five, the calculation of phase and fringe contrast, is short and does not require user interaction. Thus, it is done at the top level, in `linevisar.m` itself.

B.4   Major Analysis Step Files

The major analysis steps are listed here in the order in which they are called in `linevisar.m`. All of the `.m` files are associated with `.fig` figure files in GUI pairs with the exception of `calc_velocity.m`. The `.fig` files store the callback information for the objects within the GUI. These define which function to execute and what arguments to pass to it when a user modifies or clicks on a graphical object.

The analysis steps are written to allow the user to go back to a previous step without losing parameter settings. To accomplish this requires a few extra inputs and outputs at each step. The extra inputs are only used if a step is called a second time. On the first call, the extra inputs are initialized to an empty matrix.

B.4.1 `lv_getfiles.m`

`lv_getfiles.m` loads the data and preshot images and does some initial processing on them. A filter is applied to the shot image when the user presses "next". Most of the processing occurs immediately upon the loading of the images, in the callback `file_edit_Callback` (line 138). This callback handles the loading of both of the preshot images and the shot image, as described in subsection A.3.1.

B.4.2 `lv_time_align.m`

`lv_time_align.m` contains a three-step process that aligns the quadrature images in time, with guidance from the user, as described in subsection A.3.2.

B.4.3 `lv_position_align.m`

`lv_position_align.m` contains a three-step process that aligns the quadrature images in position, as described in subsection A.3.3.

B.4.4 `lv_lisajou.m`

`lv_lisajou.m` shows plots of the phase and allows the user to enter a phase offset. The region of interest is also set, which limits the range of the data in the following steps. This file controls the fourth major analysis step, as described in subsection A.3.4.

B.4.5 `qual_unwrap_visual.m`

`qual_unwrap_visual.m` controls the two-dimensional phase unwrapping procedure with user guidance, as described in subsection A.3.6.

B.4.6 `lv_experiment_params.m`

`lv_experiment_params.m` collects experiment parameters from the user that are necessary to compute the velocity surface, as described in subsection A.3.7.

B.4.7 `calc_velocity.m`

`calc_velocity.m` performs the calculation of velocity from the phase. This step is not interactive and thus there is no associated `.fig` file, unlike the previous steps. The calculation process is described in subsection A.3.8.

B.5 Helper functions

The following files contain helper functions which are called by the major analysis steps. They are listed in alphabetical order.

B.5.1 `amoeba.m`

`amoeba.m` is a non-linear, multi-variable function minimizer. This function was translated into MATLAB from the source code listed in the book *Numerical Recipes in C*[25]. The function mimimizer is used to automatically determine the position and time offsets in the corresponding alignment steps. The minimizer makes use of a penalty function which is computed by a separate function file. The name of the penalty function is one of the calling arguments of `amoeba.m`.

B.5.2 `cos_diff.m`

`cos_diff.m` computes a difference of the cos images, weighted by path attenuations. The computation follows Eq. 2.20.

B.5.3 `cos_sum.m`

`cos_sum.m` computes a sum of the cos images, weighted by path attenuations. The computation follows Eq. 2.22.

B.5.4 `lv_boxcar.m`

`lv_boxcar.m` performs a "boxcar", or continuous-average, filter on a signal. It is used to provide smoothed estimates of the intensity along the image boundaries in the first analysis step. The filter is modified from a standard "boxcar" to disregard the 2% of the points that are the furthest from the filtered signal. This helps to eliminate erroneous spikes in the data signals.

B.5.5 `lv_fiveBound.m`

`lv_fiveBound.m` is called by the first analysis step. It is used to find the five position boundaries of the four quadrature streak images.

B.5.6 `lv_get_response.m`

`lv_get_response.m` is called when preshot streak images are loaded in the first analysis step. This function determines the path responsivities, or attenuations, that correspond to the preshot images.

B.5.7 `lv_image_straighten.m`

`lv_image_straighten.m` is called from `lv_getfiles.m`. This function applied the boundary polynomial to correct the time-dependent position shift of the streak camera.

B.5.8 `lv_plot.m`

`lv_plot.m` produces a velocity surface plot. This function can be called independently to produce a plot from saved data.

B.5.9 `lv_pos_offset_penalty.m`

`lv_pos_offset_penalty.m` is a penalty function for use with `amoeba.m` in the position-alignment step. This penalty function computes the sharpness of the sum of all four quadrature images, allowing all three position offsets to be found simultaneously.

B.5.10 `lv_rect.m`

`lv_rect.m` is a set of callbacks that can be attached to a rectangle on a plot. These callbacks allow the user to click-and-drag the sides of the rectangle. This type of rectangle is used to set time intervals throughout the analysis.

B.5.11 `lv_time_offset_penalty.m`

`lv_time_offset_penalty.m` is a penalty function for use with `amoeba.m` in the time-alignment step. This penalty function finds only one of the three time alignment offsets at a time.

B.5.12 `lv_tilt_penalty.m`

`lv_tilt_penalty.m` is a penalty function for use with `amoeba.m` in the time-alignment step. It is used to find and correct the relative tilts of the quadrature images.

B.5.13 `sin_diff.m`

`sin_diff.m` computes a difference of the sin images, weighted by path attenuations. The computation follows Eq. 2.21.

B.5.14 `sin_sum.m`

`sin_sum.m` computes a sum of the sin images, weighted by path attenuations. The computation follows Eq. 2.23.

B.6 Parameter files

B.6.1 `optics.txt`

```
1  Material,        Wavelength, Index,    Delta
2  BK-7,            532,        1.51947,  0.03391
3  Fused Silica,    532,        1.46071,  0.032
4  BK-7,            514.5,      1.52049,  0.037
5  Fused Silica,    514.5,      1.46156,  0.034
```

`optics.txt` stores the refractive indices and delta-dispersion indices of materials that are used as delay elements, or etalons. New materials or wavelengths can be added by adding lines to this file.

B.6.2 `windows.txt`

```
1  WINDOW NAME,               (delta nu)/(nu0)
2  Free Surface,             0
3  PMMA,                     0
4  Lithium Floride <100>,    0.2566+0.0226*u
5  Fused Silica,             0.03308+0.36555*exp(-0.215*sqrt(1000*u+65.664))
6  Z-cut Quartz,             0.08107
7  C-cut Sapphire,           0.7864
8  A-cut Sapphire,           0.8693
```

`windows.txt` stores formula for the window-correction factor, $\Delta\nu/\nu$. New windows with arbitrary corrections factors may be added by adding lines to this file.

B.6.3 `default_paramaters.mat`

`default_paramaters.mat` is a binary MATLAB data file. It contains the default entries for the text boxes and pull-down menus in for the experiment parameters step.